WADC TECHNICAL REPORT 57-392
ASTIA DOCUMENT NO. AD 155543



(UNCLASSIFIED TITLE)

# TRANSONIC FLUTTER CHARACTERISTICS OF A 45 DEGREE SWEPT BACK ALL MOVABLE STABILIZER

BENJAMIN B. D'EWART JR.
ROBERT F. FARRELL

BELL AIRCRAFT CORPORATION



MAY 1958

AIRCRAFT LABORATORY
CONTRACT NO. AF 33(616)-2536
PROJECT NO. 1370

WRIGHT AIR DEVELOPMENT CENTER
AIR RESEARCH AND DEVELOPMENT COMMAND
UNITED STATES AIR FORCE
WRIGHT – PATTERSON AIR FORCE BASE, OHIO

[redacted]

## FOREWORD

The research work described in this report was performed by the Bell Aircraft Corporation, Buffalo, New York, for the Aircraft Laboratory, Wright Air Development Center, Wright-Patterson Air Force Base, Ohio. The work was accomplished under Air Force Contract No. AF33(616)-2536, Project No. 1370, (UNCLASSIFIED TITLE) "Aeroelasticity, Vibration and Noise," and Task No. 13479, (UNCLASSIFIED TITLE) "Investigation of Flutter Characteristics of All Movable Tails." Henry Katz, 1st Lt, USAF, of the Dynamics Branch, Aircraft Laboratory is task engineer. The transonic program was carried out by the Aeroelasticity Section of the Bell Aircraft Corporation Research Division, with Mr. B. B. D'Ewart, Jr. acting as project engineer, assisted by Mr. R. F. Farrell. Research started in May 1954 and is part of a continuing program of aircraft flutter research by WADC.

This document, excepting the title, is classified CONFIDENTIAL because it reveals information which can be employed to determine design criteria for the prevention of flutter of all-movable tails at transonic speeds.

[redacted]



[redacted]

## ABSTRACT

Wind tunnel tests were conducted on a family of 10 all movable 45-degree swept stabilizer models. The model panels were essentially dynamically identical except that panel stiffness levels were varied to obtain flutter within the Mach 0.8 to 1.2 speed range at a mass ratio of 25. For pitch to bending frequency ratios of 2.67 and 1.50, and a mass ratio of 25, flutter speeds remained between 16 and 19 percent higher than predicted by incompressible swept analyses using the methods of NACA TR1014. No significant transonic dip or supersonic rise in experimental values of $V_E/b_r\,\omega_\alpha$ was observed for the above conditions, however, a region of low stability was found to exist below the flutter boundary beyond Mach 1.0.

The effects of variations in pitch to bending frequency ratio with mass ratio constant at 25.0 are small and of the same order of magnitude as are predicted by reference analysis. Data points below Mach 0.92 at $\mu = 25$, show a drop of 5% in $V_E/b_r\,\omega_{h_1}$ as $\omega_\phi/\omega_{h_1}$ drops from 2.67 to 0.9 Analyses show a corresponding drop of 8%. The drop in $V_E/b_r\,\omega_{h_1}$ in going from $\omega_\phi/\omega_{h_1}$ = 2.67 to 1.50 does not exceed 7% at any point between Mach 0.8 and 1.15 at $\mu = 25.0$. Increasing mass ratio does not bring about as much of an increase in $V_E/b_r\,\omega_{h_1}$ as is predicted by incompressible analysis particularly at $\omega_\phi/\omega_{h_1} = 0.9$. At this frequency ratio at Mach 1.19 and $\mu = 70$ the incompressible analyses gave a reduced velocity that was 10 percent unconservative. Test data were not sufficient to determine the degree of interdependence of Mach number and mass ratio effects.

At Mach 0.8 the flutter to torsion frequency ratio $\omega_E/\omega_\alpha$ was from 0.55 to 0.60 and was little affected by variations in $\omega_\phi/\omega_{h_1}$. Increasing Mach number up to 1.2 at $\mu = 25$ resulted in a drop in $\omega_E/\omega_\alpha$ of about 20 percent. Increasing $\mu$ above 25 causes further drops in $\omega_E/\omega_\alpha$. For the configuration tested pitch does not become significant amplitude-wise until $\omega_\phi/\omega_{h_1}$ drops down close to unity.


## PUBLICATION REVIEW

This report has been reviewed and is approved.

FOR THE COMMANDER:

J. H. Harrington

for RANDALL D. KEATOR
Colonel, USAF
Chief, Aircraft Laboratory

TABLE OF CONTENTS

ILLUSTRATIONS

TABLES

## LIST OF SYMBOLS

| | |
|---|---|
| AR | Aspect ratio; based on area of the stabilizer exposed to the airstream |
| $C_{\phi}$ | Restraint in pitch (in.lbs./rad.) |
| EA | Elastic axis location as a fraction of a chord aft of the leading edge |
| EI | Bending rigidity (lb.in.$^2$) |
| GJ | Torsional stiffness (lb.in.$^2$) |
| $I_{\alpha}$ | Moment of inertia of the stabilizer about the elastic axis per unit span (lb.in.$^2$)/in. |
| $I_{\phi}$ | Moment of inertia about the pitch axis (lb.in.$^2$) |
| K | Distance from elastic axis to pitch axis measured along the stabilizer root chord at fuselage fairing line taken in the streamwise direction (positive for pitch axis aft of EA) |
| $M_E$ | Free stream test Mach number at flutter |
| $P_o$ | Total head pressure in wind tunnel (lbs./ft.$^2$) |
| $S_{\alpha}$ | Static moment of the stabilizer per unit span about the elastic axis; positive when the c.g. is aft of the elastic axis (lb.-in.)/in. |
| $V_R$ | Analysis flutter speed computed using two-dimensional incompressible air flow; (ft./sec.) |
| $V_E$ | Test speed at flutter; parallel to the airstream (ft./sec.) |
| $k = \frac{\omega b_r}{V_R}$ | |
| q | Dynamic pressure (lbs./ft.$^2$) |
| $r_{\alpha}$ | Radius of gyration of the stabilizer perpendicular to the EA, expressed as a fraction of the stabilizer semichord |
| $t_o$ | Stagnation temperature in the wind tunnel (°F) |
| $x_{\alpha}$ | Distance from the elastic exis to the center of gravity measured on a line perpendicular to the EA expressed as a fraction of the stabilizer semichord; positive when the c.g. is aft of the EA |
| $V/b_r \omega_{\alpha}$<br>$V/b_r \omega_{h_i} \sqrt{\mu}$ | Reduced Flutter velocity of stabilizer |
| w | Weight of the stabilizer per unit span (lbs./in.) |
| b | Local semichord of a stabilizer measured perpendicular to the EA |
| $b_r$ | Reference Semi-Chord measured parallel to airstream at 75% of exposed semi-span |

| | |
|---|---|
| $f$ | Flutter frequency (cps) |
| $f_{h_i}$ | a) $i^{th}$ uncoupled bending mode shape normalized to unity at intersection of EA and stabilizer tip |
| | b) the symbol $f_{h_i}$ also employed to designate the uncoupled bending frequency in the $i^{th}$ mode (cps) |
| $f_{\alpha_i}$ | a) $i^{th}$ uncoupled torsion mode shape normalized to unity at intersection of EA and stabilizer tip |
| | b) the symbol $f_{\alpha_i}$ also employed to designate the uncoupled torsion frequency in the $i^{th}$ mode (cps) |
| $f_{\phi} = 1$ | Pitch mode shape |
| $g$ | Structural damping coefficient considered as a variable in the solution of the flutter determinant |
| $\Lambda$ | Sweepback angle of the elastic axis |
| $\mu$ | Ratio of the mass of a unit length (parallel to the elastic axis) of the stabilizer to the mass of a corresponding unit length of a cylinder of air with its diameter equal to the stabilizer chord measured perpendicular to the elastic axis, taken at 75% of exposed semi-span |
| $\rho_E$ | Density of air at a model during a wind tunnel test (slugs/ft.$^3$) |
| $\rho_R$ | Reference air density required to give $\mu$ =25. (slugs/ft$^3$) |
| $\omega_{h_i}$ | Uncoupled bending frequency in the $i^{th}$ mode (rad./sec.) |
| $\omega_{\alpha_i}$ | Uncoupled torsion frequency in the $i^{th}$ mode (rad./sec.) |
| $\omega_{\phi}$ | Uncoupled pitch frequency (rad./sec.) |
| $\omega_i$ | Frequency of the $i^{th}$ coupled mode (rad./sec.) |
| $\omega_R$ | Analysis flutter frequency computed using two-dimensional incompressible airflow (rad./sec.) (Ref. 1) |
| $\omega_E$ | Frequency of flutter at test flutter Mach number (rad./sec.) |
| $\Omega =$ | $(\omega_\alpha/\omega)^2 \quad (1 + jg)$ |

## INTRODUCTION

There has been a definite trend towards utilization of all-movable control surfaces on modern high speed aircraft to obtain increased control effectiveness. However, the use of this type of control clearly increases the possibility of flutter problems as is substantiated by the fact that at least seven cases of flutter of this type of surface are known to have occurred on U.S. aircraft and missiles within the last four years. This has pointed up the need for a better understanding of, and control over, the parameters contributing to flutter of these surfaces. This report summarizes wind tunnel test data in the Mach 0.8 to 1.2 speed range on a family of 10 all movable stabilizer models of 45 degree quarter chord sweep. Model geometry, mass and elastic characteristics are summarized in Section 1 of this report. These characteristics are typical of existing aircraft configurations. Design and construction details are presented in Appendix I. Model calibration and data reduction procedures are covered in Appendix II.

Testing was accomplished using the WADC 10 ft. Transonic Tunnel. Models were mounted from a side wall of the test section.

Flutter analyses were performed using incompressible two-dimensional air force coefficients in analyses utilizing the methods of NACA TR 1014 (Ref. 1). Analysis results are summarized in Section 2. Presentation of flutter test results is made in Section 3. A discussion of these results and a comparison of analysis and test results is also made in Section 3.

---

Manuscript released by the Authors April 1958 for publication as a WADC Technical Report.

[redacted]

## SECTION I

## MODEL CHARACTERISTICS

The general features of the test configurations are shown in Figure 1. The 10 models tested were geometrically identical and had similar mass and elastic characteristics except that model stiffness levels were varied to allow flutter within the Mach 0.8 to 1.2 speed range at a mass ratio of 25. Flexure pivots provided a pitch degree of freedom through the 35.0% MAC based on span to fuselage centerline. By using two flat torsion springs with variable effective lengths, pitch frequency could be varied from 33 cps to 214 cps. Data was taken almost entirely at pitch to bending frequency ratios of 0.9, 1.5 and 2.67. A method was provided for locking out the pitch degree of freedom to allow the stabilizer models to be checked as cantilevers. General model characteristics are summarized beneath Figure 1. Important parameters of the individual models are summarized in Table I. Model dimensions, construction details, etc. are covered in Appendix 1.

A half fuselage of 5-inch radius was provided to reduce tunnel boundary layer effects. The test assembly was mounted from a side wall of the WADC 10 ft. Transonic Tunnel. One of the tunnel's circular windows was replaced with a steel plate to which the model supporting structure, operating mechanisms, and fuselage section were attached. The window frame contained a drive mechanism which allowed the rotation of the entire assembly for streamlining the models.

Models were provided with bending-sensitive and torsion-sensitive strain gage bridges for use in determining flutter frequencies and amplitude ratios. The flexure pivots in the pitch system were also strain gaged to provide corresponding data for pitch. Details of model construction and calibration are given in Appendix II.



[redacted]

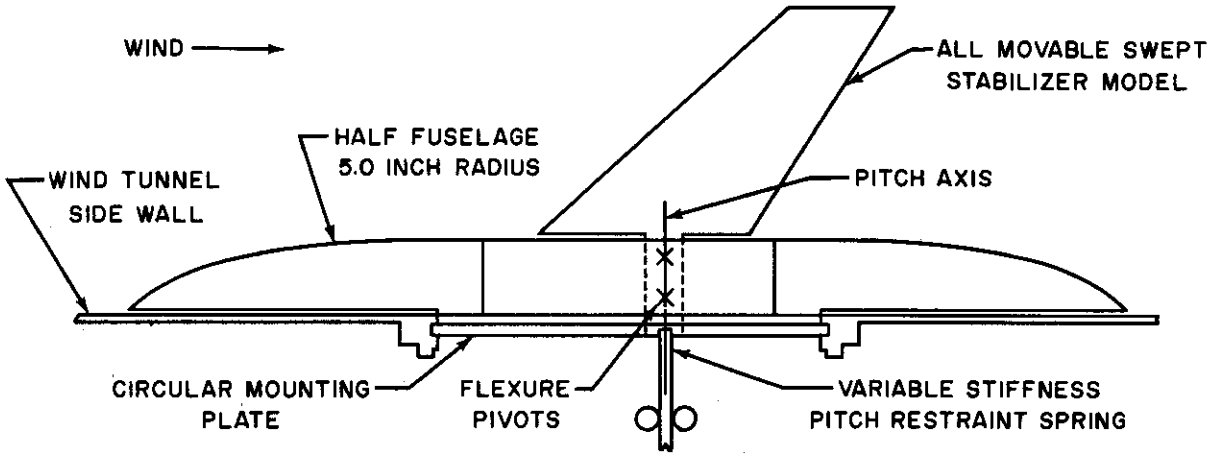


Figure 1. General Model Testing Configuration Used in WADC 10 Ft Transonic Tunnel

MODEL CHARACTERISTICS:

| | |
|---|---|
| Quarter Chord Sweep | 45. Deg. |
| Taper Ratio of External Span | 0.5 |
| Aspect Ratio of External Span | 2.91 |
| Airfoil | NACA 65 A004 In Wind Direction |
| Pitch Axis Location: | 35.0% MAC Based on Span to Fuselage Centerline |
| | or |
| | 60.4% Root Chord in Wind Direction at Surface of Fuselage |

E.A. 41.6% Chord Normal to Quarter Chord
c.g. 50% Chord Normal to E.A.
For detailed dimensions see Appendix I
Range of Torsion Frequencies of 10 Models Tested, 153 to 219 cps
Average Bending To Torsion Frequency Ratio 0.273
Variable Pitch Frequency Range 33 to 214 cps
For Mass and Elastic Characteristics of Each Model See Table I

TABLE I

SUMMARY OF MODEL CHARACTERISTICS

| Model | $f_{h_1}$ (cps) | $f_{h_2}$ (cps) | $f_{\alpha_1}$ (cps) | $f_{\alpha_2}$ (cps) | $f_{h_1}/f_{\alpha_1}$ | $\rho$ At $\mu$ =25 Slugs/Ft$^3$ | $I_\phi$ lb in 2 (Stab. Only) | $x_\alpha$ AV | $r^2_\alpha$ AV | $EA_{AV}$ % Chord From L.E. | $CG_{AV}$ % Chord From L.E. |
|---|---|---|---|---|---|---|---|---|---|---|---|
| 1 | 51.0 | 194.3 | 187.8 | 394.0 | .272 | .001352 | 20.80 | .170 | .250 | 41.5 | 50 |
| 2 | 52.0 | 198.2 | 189.0 | 397.0 | .275 | .001352 | 20.80 | .176 | .250 | 41.2 | |
| 3 | 43.2 | 177.5 | 156.5 | 332.0 | .276 | .001468 | 22.84 | .173 | .248 | 41.3 | |
| 4 | 42.5 | 172.5 | 153.5 | 320.5 | .277 | .001428 | 22.55 | .165 | .246 | 41.7 | |
| 5 | 55.4 | 210.7 | 199.0 | 418.0 | .278 | .001352 | 20.80 | .190 | .250 | 40.5 | |
| 6 | 59.0 | 222.1 | 219.0 | 460.0 | .270 | .001352 | 20.80 | .158 | .250 | 42.1 | |
| 7 | 46.1 | 185.2 | 166.3 | 345.0 | .277 | .001211 | 19.65 | .162 | .246 | 41.9 | |
| 8 | 47.3 | 190.5 | 177.5 | 371.0 | .266 | .001195 | 19.08 | .176 | .243 | 41.3 | |
| 9 | 52.0 | 210.0 | 189.0 | 400.0 | .275 | .001150 | 18.27 | .161 | .250 | 41.9 | |
| 10 | 55.9 | 227.0 | 209.0 | 439.0 | .267 | .001279 | 19.67 | .153 | .246 | 42.3 | 50 |
| Averages | | | | | .273 | | 20.53 | .168 | .248 | 41.6 | 50 |

Pitching inertia of all elements of pitch system behind fuselage fairing ≈ 2.05 lb in$^2$ (varies slightly with effective pitch spring length) see Fig. 25

## SECTION 2

## FLUTTER ANALYSES

Four degree of freedom flutter analyses were performed to provide the usual incompressible flow "reference analysis" data for use as a basis of comparison of analysis versus experiment. First bending, torsion, second bending and pitch degrees of freedom were used. Uncoupled pitch to bending frequency ratios and mass ratio were varied over the range of conditions encountered in the test program.

Analyses were performed using for $x_\alpha$ the original design value of 0.20. Since laboratory tests showed variations in $x_\alpha$ down to 0.15 a number of check points for $x_\alpha$ = 0.17 and 0.15 were made. Resulting variations in $V_R/b_r\omega_\alpha$ were 1.0% or less.

Development of the flutter equations follows the general methods outlined in NACA Report 1014 (Reference 1) expanded to include the pitch and second bending modes. Secondary spanwise flow terms as indicated in Reference 1 by heavy brackets have been omitted in accordance with common practice. Analysis details and a summary of determinant elements are given in Appendix III.

Analysis results are summarized in Figures 2 through 6 which show the flutter parameters as functions of mass ratio and $\omega_\phi/\omega_{h_1}$. Figure 2 shows the variations in $V_R/b_r\omega_\alpha$ with mass ratio and pitch to bending frequency ratio. Going from $\mu$ = 25 to $\mu$ = 75 at constant $\omega_\phi/\omega_{h_1}$ causes a 43 to 54 percent increase in $V_R/b_r\omega_\alpha$ depending on the value of $\omega_\phi/\omega_{h_1}$ while a change in $\omega_\phi/\omega_{h_1}$ from 0.9 to $\infty$ at constant $\mu$ causes only a 10 to 17 percent increase in $V_R/b_r\omega_\alpha$ depending on the value of $\mu$. Figure 3 shows that a change in mass ratio from 25 to 70 while holding $\omega_\phi/\omega_{h_1}$ constant causes a 16 to 26 percent drop in $\omega_R/\omega_\alpha$ depending on the value of $\omega_\phi/\omega_{h_1}$, while a change in $\omega_\phi/\omega_{h_1}$ from 0.9 to $\infty$ at constant $\mu$ causes a 26 to 44 percent increase in $\omega_R/\omega_\alpha$.

The reference analyses show flutter for a given model ($b_r\omega_{h_1}$ = a constant) as a function of true airspeed V and mass ratio $\mu$. Selecting $V/b_r\omega_{h_1}\mu^x$ as a flutter index, x may be solved for to make this index a constant between specified values of $\mu$. Experience to date indicates that x will lie between 0.5 and 0.0. When x = 0.5, the index becomes the familiar $V/b_r\omega_{h_1}\sqrt{\mu}$ which has the special feature of being a function of q. Thus, a constant value of this flutter index for a given model or airplane indicates a constant q flutter. x approaching zero indicates decreasing sensitivity of flutter speed to changes in mass ratio, with velocity becoming invariant at x = 0 for a given model. Since stability then depends only on true airspeed, this limiting condition has been called a true airspeed flutter. For a family of models differing only in natural frequencies, $V/b_r\omega_{h_1}$ rather than V would be invariant for the true airspeed flutter condition.

Solving for x as indicated above using the data of Figure 2 over increments of mass ratio of 10.0 gave values of x ranging from 0.47 at $\mu$ = 25 range down to 0.28 at $\mu$ = 70, for $\omega_\phi/\omega_{h_1} = \infty$ and corresponding values of x from 0.42 to 0.20 for $\omega_\phi/\omega_{h_1}$ = 0.9. Figure 4 shows the variations in $V_R/b_r\omega_{h_1}\sqrt{\mu}$ over the $\mu$ range used in testing. If analyses predicted constant q flutter, the curves of Figure 4 would be straight horizontal lines. A constant q flutter would show up on Figure 2 as indicated by the dotted line for the $\omega_\phi/\omega_{h_1} = \infty$ case based on the value of $V_R/b_r\omega_{h_1}$ at $\mu$ = 25. Figure 5 shows the drops in q at flutter relative to the value at $\mu$ = 25 which occur as $\mu$ is varied from 25 to 70.

To show the small sensitivity of $V_R/b_r\omega_{h_1}$ to changes in pitch to bending frequency ratio, Figure 4 has been crossplotted to give Figure 6.

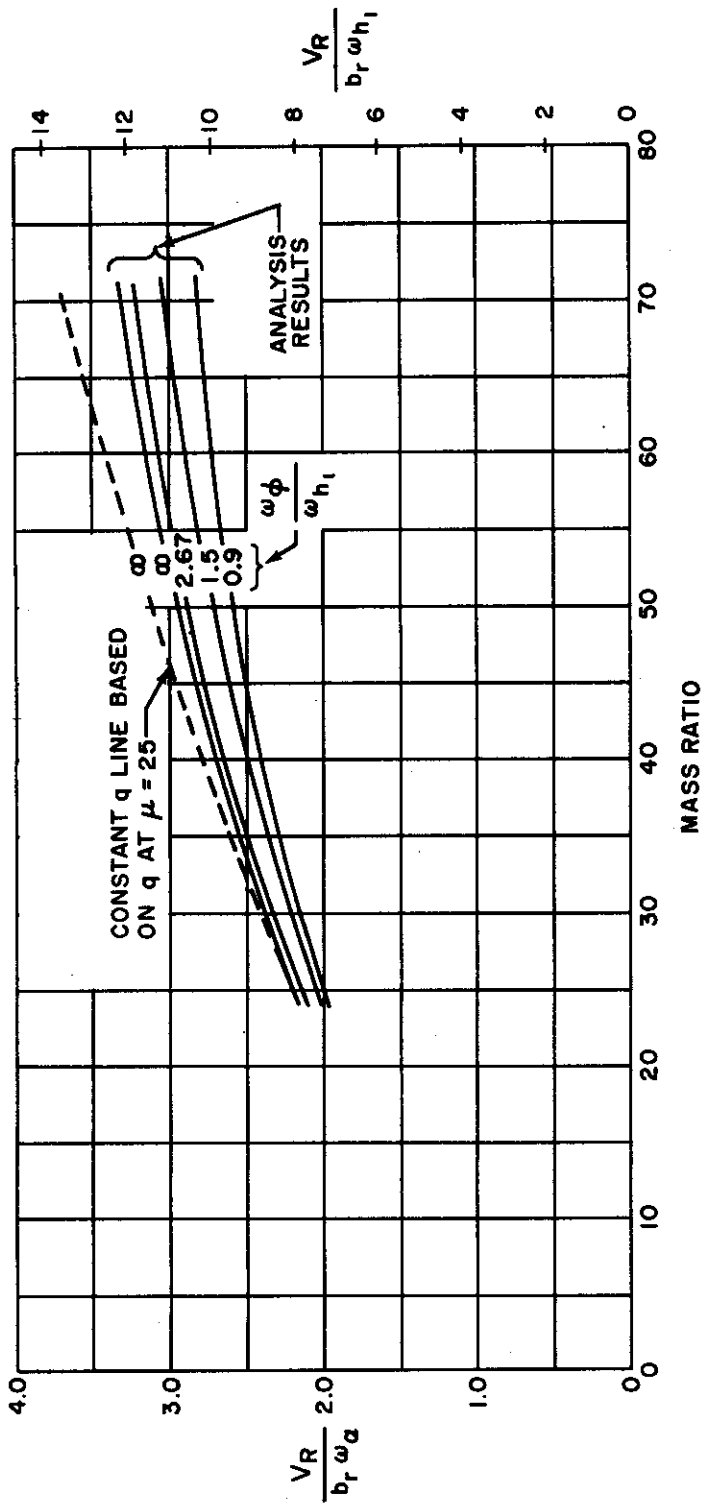


Figure 2. Analysis results, $V_R/b_r\omega_\alpha$ versus mass ratio for pitch to bending frequency ratios used in testing. Dotted line indicates constant q flutter (i.e. $V_R/b_r\omega_\alpha\sqrt{\mu} = a$ (constant) with $\omega_\phi/\omega_{h_1} = \infty$, based on $V_R/b_r\omega_{h_1}$ at $\mu = 25$

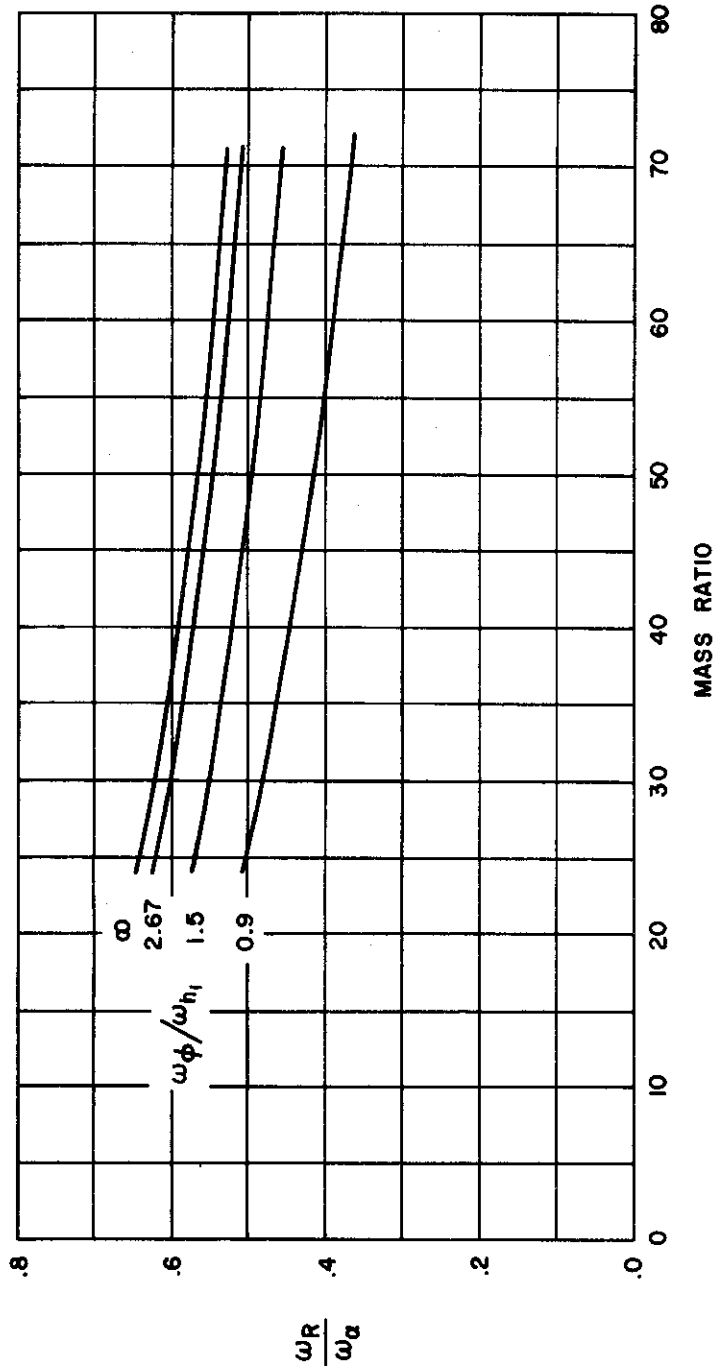


Figure 3. Analysis results, flutter to torsion frequency ratio versus mass ratio for pitch to bending frequency ratios used in testing.

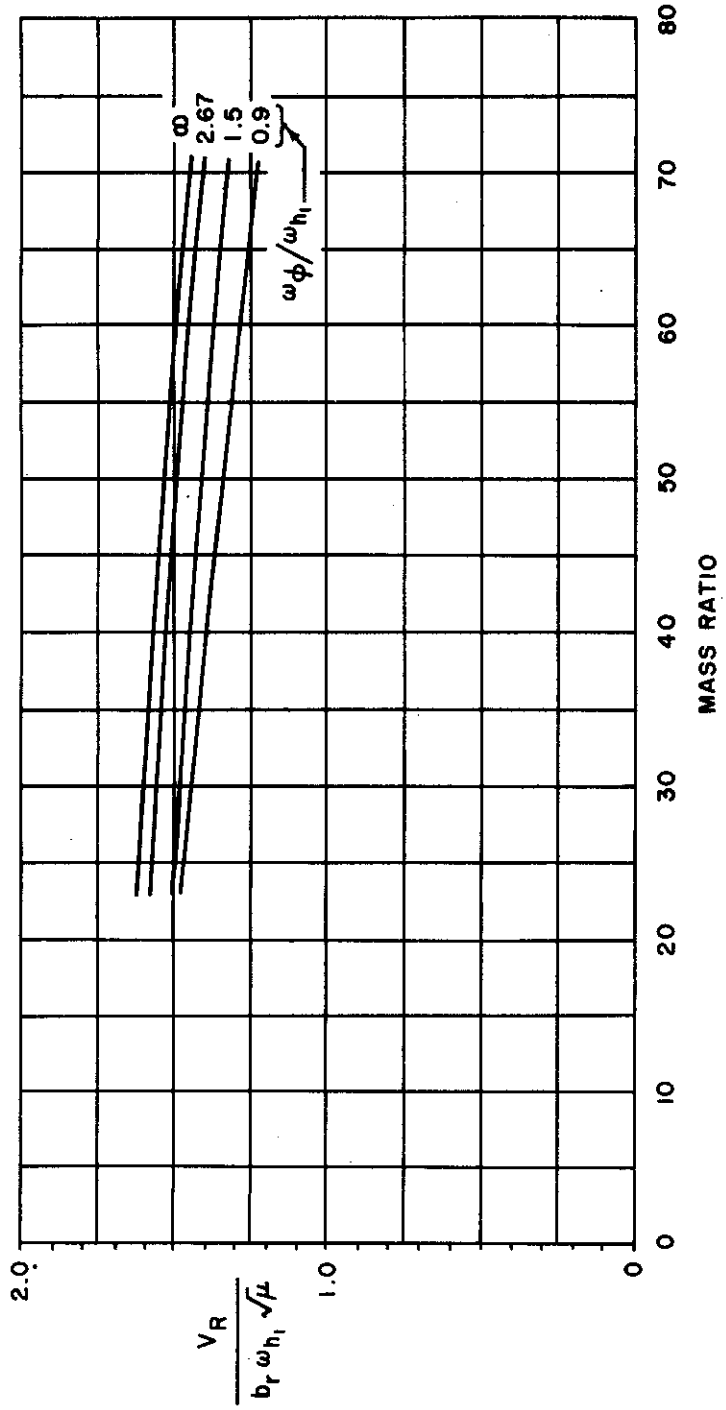


Figure 4. Analysis results $V_R/b_r\omega_{h_1}\sqrt{\mu}$ versus mass ratio for pitch to bending frequency ratios used in testing.

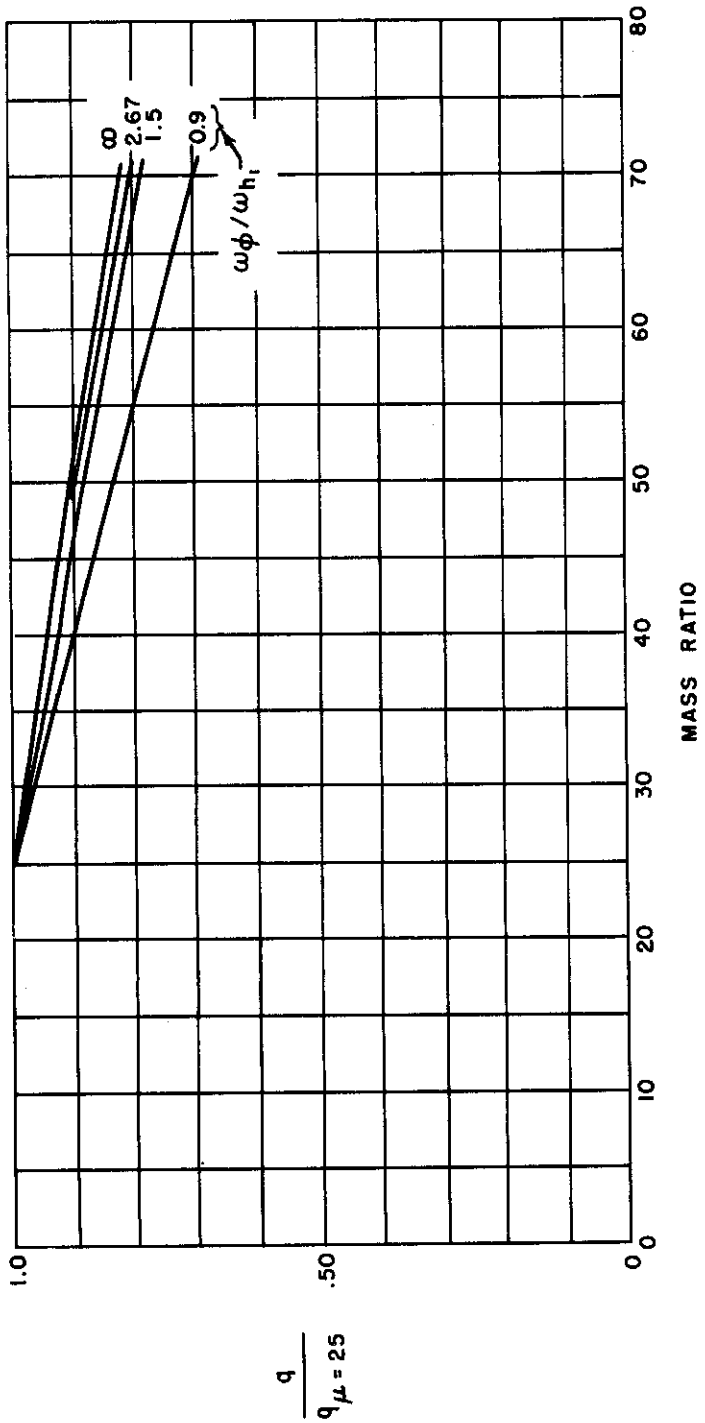


Figure 5. Analysis results, variations in q as a ratio with the value at $\mu$ = 25 versus mass ratio for pitch to bending frequency ratios used in testing.

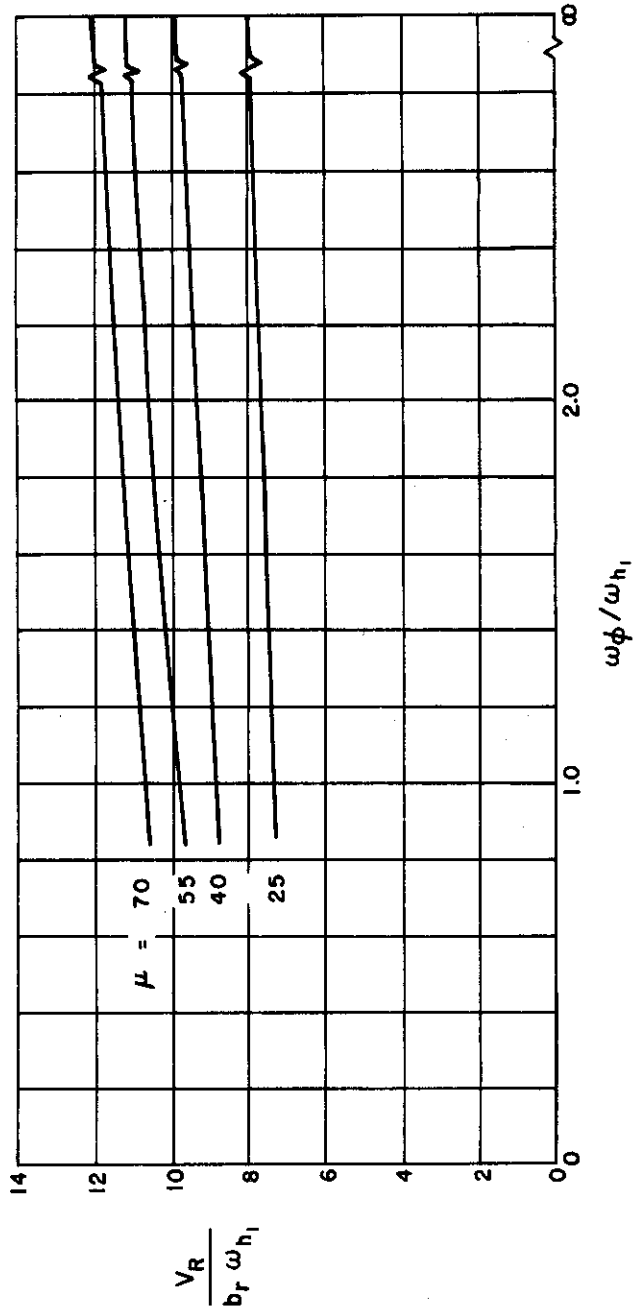


Figure 6. Analysis results crossplot of Figure 2 showing small sensitivity of $V_R / b_r \omega_{h_1} \sqrt{\mu}$ to variations in $\omega_\phi / \omega_{h_1}$

## SECTION 3

## TEST RESULTS

### 1. Presentation of Data

A summary of test data is given in Table IV. With one exception test points were limited to pitch to bending frequency ratios $\omega_\phi/\omega_{h_1}$ of 0.9, 1.5, 2.67 and $\infty$. The data at these frequency ratios is plotted on Figures 7 through 10 in terms of the parameter $V_E/b_r\,\omega_{h_1}\sqrt{\mu}$. As much data as possible was obtained at a mass ratio $\mu$ of 25 to eliminate this parameter as a test variable. Tests were conducted at high mass ratios in some cases to get flutter at high Mach numbers where frequencies of available models were too low to give the desired test speed at $\mu = 25$. In such cases the desired Mach number was held and test density was increased to get flutter. Figure 11 shows all data in terms of the reduced velocity parameters $V_E/b_r\,\omega_{h_1}$ and $V_E/b_r\,\omega_\alpha$.

In considering the high mass ratio points on Figure 11 it should be realized that at a given Mach No., the ordinates are a function of $\omega_h$, $\mu$, and $\omega_\phi/\omega_{h_1}$. Therefore conclusions as to the effects of any one of the variables can be made only for those limited cases where the other variables were held constant. Ratios of experimental flutter velocities to corresponding analysis velocities were obtained using the analysis data of Section 2. These velocity ratio data are shown graphically in Figure 12. The average value of the speed of sound at the test section was 1060 ft/sec and the average deviation from this value was 1.2%.

A high degree of tunnel turbulence plus the large region of very low stability below the true flutter boundary in the transonic region made the identification of the true flutter boundary very difficult, time consuming and costly in models, and was a major factor in limiting the total number of data points obtained. Sufficient data were obtained at pitch to bending frequency ratios of 1.5 and 2.67 at a mass ratio of 25 to allow trend curves to be drawn for the respective $V_E/b_r\,\omega_{h_1}\sqrt{\mu}$ plots of Figures 8 and 9. $\mu = 25$ data at these two frequency ratios on Figure 10 through 12 has been represented by the trend curves rather than by the data points. Data at other frequency ratios occurred over such a range of mass ratios and were so sparse that trend curves were not attempted. The separate data points are therefore shown and individually identified on Figures 10 through 12.

Flutter frequencies are shown ratioed with their respective torsion frequencies and analyses flutter frequencies in Figures 15 and 16 respectively. Amplitude ratio data are presented in Figure 17.

### 2. Discussion

#### a. Data at $\omega_\phi/\omega_{h_1} = 0.9$

Since data at this frequency ratio were considered of less practical importance for present day aircraft than data at higher frequency ratios, tests at this frequency ratio were given a low priority. As a result only 3 flutter points were obtained as shown on Figure 7. The large increases in the mass ratios (necessary to get models 8 and 10 to flutter supersonically at this low pitch to bending frequency ratio) caused a pronounced drop in $V_E/b_r\,\omega_{h_1}\sqrt{\mu}$ as the Mach number was increased.

Test points at Mach 0.80 and 1.05 involved a simultaneous change in 3 variables: $\omega_{h_1}$, Mach number and $\mu$, making trend observations difficult. The Mach 1.05 and 1.19 test points were obtained using the same model, and therefore these two test points may be considered as showing the

effect of a change in speed and altitude on a given stabilizer. Going from Mach 1.05 to 1.19 represents a 13.3% increase in Mach number. However, due to a 33°F drop in tunnel stagnation temperature plus the increased temperature drop due to the expansion to the higher Mach number, the corresponding increase in velocity and hence $V_E/b_r\,\omega_{h_1}$ was only 2.0%. This indicated velocity increase combined with the change in mass ratio from 40.1 to 70.9 resulted in a 40% drop in dynamic pressure. The reference analysis predicts a 17% increase in $V_R/b_r\,\omega_{h_1}$ for an increase in $\mu$ from 40.1 to 70.9%. The failure of this large increase in reduced velocity to show up experimentally points toward an unconservative tendency in "reference" analyses as $\mu$ is increased and/or the existance of a large destabilizing compressibility effect acting at this pitch to bending frequency ratio. Additional data points at $\mu$ = 25, 40 and 70 throughout the entire high subsonic and transonic speed range would be valuable in isolating compressibility and mass ratio effects.

b. Data at $\omega_\phi/\omega_{h_1}$ = 1.5

At a mass ratio of 25 a flutter boundary has been established as shown on Figure 8. For this mass ratio and frequency ratio the possibility of a "transonic dip" between Mach 0.95 and 1.15 (where actual flutter points are lacking) is eliminated by virtue of the test sequence used in arriving at the Mach 1.18 test point (model 6, $\mu$ = 28.0). The test path is plotted on Figure 8 as a phantom line. It is seen to approach the $\mu$ = 25 flutter boundary along a tangential path through the transonic region. Since the mass ratio along this path was always in the vicinity of 25, any pronounced "transonic dip" would have caused flutter to appear at a considerably lower Mach number than was found to be the case. Reference 3 reports a small dip for similar swept cantilever models at $\mu$ = 25. The data point obtained on model 6 at Mach 1.18 was a well defined divergent flutter. Figure 13 is a section of oscillograph record from this run just before the model was lost. Since it occurred at virtually the same value of $V_E/b_r\,\omega_{h_1}\,\sqrt{\mu}$ as did the subsonic data points, no significant supersonic rise of the type reported in Reference 3 for similar swept cantilevered models seems to exist at $\mu$ = 25 for this pitch to bending frequency ratio and Mach range.

A very low stability region below the flutter boundary was found to exist above Mach 1.0 for $\mu$ greater than 25. This has been indicated in Figure 8 as a dotted area. Models in this region always appeared to be very close to flutter while mass ratios were always above 25 and sometimes above 50. Even though models were near flutter throughout this region it was usually necessary to make large changes in mass ratio to cause actual flutter, thus indicating a low sensitivity to density changes.

Comparing Figure 8 with Figure 7, it appears that the low stability at $\omega_\phi/\omega_{h_1}$ = 1.5 shown in Figure 8 is altered to a condition of instability when $\omega_\phi/\omega_{h_1}$ is dropped to 0.9 causing flutter to occur along the lower side of what was the low stability regions for $\omega_\phi/\omega_{h_1}$ = 1.5. The $\mu$ = 45.4 data point obtained on model 7 at Mach 1.05 was obtained by holding Mach number constant and slowly increasing test density (moving straight up on Figure 8). The model fluttered to destruction at the point indicated. The $\mu$ = 38.9 data point shown for model 10 at Mach 1.18 was obtained in the same manner; however, the test was stopped before the model attained a divergent flutter. Going from this data point to the Model 6 data point at Mach 1.18 and $\mu$ = 28.0 represents a drop in $\mu$ of 28% with an accompanying drop in $V_E/b_r\,\omega_{h_1}$ of only 4%. A minor drop in reduced velocity (increased stability due to increased $\omega_{h_1}$) is equivalent here to a large drop in mass ratio (decreased stability due to larger aerodynamic forces). Solving for the value of x which makes the flutter index $V_E/b_r\,\omega_{h_1}\,\mu^x$ a constant for these two flutter points gives x = 0.11. The two flutter points therefore indicate flutter in this test region to be more nearly a function of true airspeed than q, since constant q flutter requires that x = 0.5 in the above flutter index (see bottom half of Page 5). These two test points and other high mass ratio points are also shown on the $V_E/V_R$ plot of Figure 12 illustrating the decrease in conservatism of "reference" analysis relative to test as mass ratio is increased. It appears that this loss of conservatism of "reference" analyses with increasing mass ratios is due to the relatively small increase in $V_E/b_r\,\omega_{h_1}$ observed experimentally with increasing $\mu$ as compared with reference analysis predictions. While experimental data is insufficient to prove that contributions from compressibility and pitch to bending frequency ratio are not significant in this

connection, such a conclusion is given some weight by the fact that the trend curves for $\omega_\phi/\omega_{h_1} = 1.5$ and 2.67 show that the effects due to these factors are small at $\mu = 25$. Additional data points at the higher mass ratios would be of great value in establishing flutter boundaries at higher mass ratios, however, such tests were beyond the scope of the contract and were not feasible with available models.

c. Data at $\omega_\phi/\omega_{h_1} = 2.67$

Data obtained at this frequency ratio are shown on Figure 9. The flutter boundary for $\mu = 25$ is defined up to Mach 1.05 by the data from models 2 and 3. A sequence of run points obtained for model 6 at $\mu = 25$ and $\omega_\phi/\omega_{h_1} = 2.64$ shown as a phantom line, has been plotted between Mach 1.05 and 1.15. During this sequence the model was observed to be closest to flutter at Mach 1.09. Examination of the oscillograph records indicated that the model had not quite reached flutter. The $\mu = 25$ curve of Figure 9 has, therefore, been passed above this test sequence line, but parallel to it at Mach 1.09. As in the $\omega_\phi/\omega_{h_1} = 1.5$ case no significant transonic dip is indicated. Model 6 showed a decreasing flutter tendency above Mach 1.09 indicating a definite rise in the $\mu = 25$ flutter boundary above Mach 1.09.

Figure 9 shows a low stability region as a dotted area between Mach 1.0 and 1.2 below the $\mu = 25$ flutter boundary. Mass ratios of models in this region ranged from 25 to 80. The $\mu = 35$ point for model 10 at Mach 1.18 was obtained by holding Mach number constant and slowly increasing tunnel density (moving up on Figure 9). The test was stopped at the test point indicated as flutter seemed imminent. As in the $\omega_\phi/\omega_{h_1} = 1.5$ case raising mass ratio above 25 thus appears to drop the flutter boundary (in terms of the parameter $V_E/b_r\,\omega_{h_1}\sqrt{\mu}$ ) at low supersonic speeds.

d. Data at $\omega_\phi/\omega_{h_1} = \infty$

A minimum of testing was done with the pitch degree of freedom locked out in view of the relatively plentiful amount of data available for swept cantilever wings. Consequently only two data points were obtained to allow some correlation of pitch flutter data with this limiting case. To get flutter in the desired speed range, Mach number was set and flutter was approached by raising tunnel density. Flutter occurred at mass ratios of 34.8 and 35.7 at Mach numbers of 1.0 and 1.06, respectively. The points are plotted on Figure 10 in terms of $V_E/b_r\,\omega_{h_1}\sqrt{\mu}$. This figure also shows the $\mu = 25$ trend lines for $\omega_\phi/\omega_{h_1} = 2.67$ and 1.5 and the three data points at $\omega_\phi/\omega_{h_1} = 0.9$ for comparative purposes. The drop in $V_E/b_r\,\omega_{h_1}\sqrt{\mu}$ accompanying increasing mass ratio above 25 which has been demonstrated for $\omega_\phi/\omega_{h_1} = 1.5$ and 2.67 is undoubtedly the reason why these two data points for $\omega_\phi/\omega_{h_1} = \infty$ do not fall above the $\omega_\phi/\omega_{h_1} = 2.67$ trend line for $\mu = 25$.

A transonic dip followed by a pronounced supersonic rise in $V_E/b_r\,\omega_\alpha$ is reported in Reference 3 for swept cantilever wings of aspect ratio 3.1, taper ratio 0.4, and $\omega_h/\omega_\alpha = 0.2$. The models of this program do not seem to show evidence of this trend, however the limited cantilever data of this program and differences between models of the two programs may make a comparison unjustified.

3. Effect of Pitch Frequency on Flutter Speed

To show the experimentally observed relationship between pitch to bending frequency ratio with a minimum of compressibility influence, all data points up to Mach 0.92 were plotted in Figure 13 showing $V_E/b_r\,\omega_{h_1}$ versus $\omega_\phi/\omega_{h_1}$ . These data were for mass ratios between 23.5 and 24.6. The drop in $\omega_\phi/\omega_{h_1}$ from 2.67 to 0.9 causes a drop in $V_E/b_r\,\omega_{h_1}$ of 5%. Analysis values of $V_r/b_r\,\omega_{h_1}$ versus $\omega_\phi/\omega_{h_1}$ from Figure 6 are also shown on Figure 13 for comparison. The analysis curve at $\mu = 25$ shows a drop in $V_R/b_r\,\omega_{h_1}$ of 6% between $\omega_\phi/\omega_{h_1} = 2.67$ and 0.9. In this frequency ratio and Mach number range the experimental reduced velocities average 7.5 percent higher than analysis values.

Figure 11 indicates that for $\omega_\phi/\omega_{h_1}$ between 1.5 and 2.67 the effects of pitch frequency on $V_E/b_r\,\omega_{h_1}$ are not significantly altered by compressibility effects in the transonic range, i.e. the $\mu =$

25 curves at the two frequency ratios are roughtly straight and parallel through the entire transonic region. From Mach 0.95 to 1.20 the drop in $V_E/b_r\,\omega_{h_1}$ in going from $\omega_\phi\ \omega_{h_1} = 2.67$ to 1.5 does not exceed 7%. Figure 6 shows a 4.0 percent drop in the corresponding "reference" analysis values, indicating a general correspondence between test and "reference" analysis.

The effects of going from $\omega_\phi/\omega_{h_1} = 2.67$ to $\infty$ and from $\omega_\phi/\omega_{h_1} = 1.5$ to 0.9 can not be accurately established due to the simultaneous variations in Mach number and mass ratio, and the sparsity of test points at $\omega_\phi/\omega_{h_1} = 0.9$ and $\infty$ . Additional testing should be done at these frequency ratios holding mass ratio constant to allow quantitative observations of the separate effects of pitch to bending frequency ratio and mass ratio through the transonic range.

4. Flutter Frequency Characteristics

Flutter frequencies are shown ratioed to model torsion frequencies and analysis flutter frequencies in Figures 15 and 16 respectively. Considering the $\mu = 25$ data, a drop of about 20% occurs in $\omega_E/\omega_\alpha$ as Mach number increases from 0.75 to 1.2 with the greater part of the drop occurring between Mach 0.75 and 0.90. This would indicate a more prominent participation of the bending mode as substantiated to a limited extent by the amplitude ratios. Higher mass ratios cause a progressively greater drop in $\omega_E/\omega_\alpha$ . The extreme case occurs at $\omega_\phi/\omega_{h_1} = 0.9$ where the combined effects of Mach number and $\mu$ increase from 24.5 to 70.9 are to cause a drop in $\omega_E/\omega_\alpha$ of 45%.

This mass ratio trend disappears in the $\omega_E/\omega_R$ plot of Figure 16 indicating a reasonable analytical predication of mass ratio effects on frequency. Analysis appears to predict the proper flutter frequency in the vicinity of Mach 0.8 ($\omega_E/\omega_R = 1.0$). Since the analyses performed do not account for compressibility effects ($\omega_R$ is not a function of Mach number) the drop in $\omega_E/\omega_\alpha$ observed in Figure 14 is repeated in Figure 15.

5. Amplitude Ratios and Phase Angles

Both analytical and experimental amplitude ratios and phase angles are presented in Figure 17. As may be seen, analysis predicts a phase shift of $\phi$, $\alpha$ and $h_2$ from a roughly in phase condition relative to $h_1$ to a nearly out of phase condition as $\omega_\phi/\omega_{h_1}$ drops from 3.0 to 0.5. Analytical amplitude ratios are seen to increase in the region $1.0 \leq \omega_\phi/\omega_{h_1} \leq 2.0$ and then to decrease at very low $\omega_\phi/\omega_{h_1}$ with the exception of $\phi/\alpha$ which continues to increase as $\omega_\phi/\omega_{h_1}$ decreases.

In establishing experimental values from strain gage data the peaks of the traces were examined first of all to ascertain the relative phasing. At $\omega_\phi/\omega_{h_1} = 2.67$ and generally at $\omega_\phi/\omega_{h_1} = 1.5$ the phasing between the peaks of traces was either negligible or was of the same order of magnitude as the estimated reading error. Accordingly, amplitude ratios were established for most data points assuming zero phasing. For model 4, however, at $\omega_\phi/\omega_{h_1} = 1.5$ and for the three data points at $\omega_\phi/\omega_{h_1} = 0.9$ phasing between peaks appeared to be significant and was accounted for in arriving at amplitude ratios. The general increases in $\phi$, $\alpha$, and $h_2$ relative to $h_1$ as $\omega_\phi/\omega_{h_1}$ drops toward 0.9 indicates a replacement of the bending motion by a more prominent pitch motion as $\omega_\phi/\omega_{h_1}$ drops.

TABLE II — TEST DATA SUMMARY

| MODEL | 1 | 2 | | 3 | 4 | 6 | | 7 | 8 | | | | 9 | 10 | | | |
|---|---|---|---|---|---|---|---|---|---|---|---|---|---|---|---|---|---|
| $f_\alpha$ ~cps | 187.8 | 189.0 | | 156.5 | 153.5 | 219.0 | | 166.3 | 177.5 | | | | 189.0 | 209.0 | | | |
| $f_{h_1}$ ~cps | 51.0 | 52.0 | | 43.2 | 42.5 | 59.1 | | 46.1 | 47.3 | | | | 52.0 | 55.9 | | | |
| $\rho_R$ slugs/ft$^3$ | .001352 | .001352 | | .001468 | .001428 | .001352 | | .001211 | .001195 | | | | .001150 | .001279 | | | |
| Test Point | 19 | 167 | 171 | 38 | 5 | 115 | 111 | 30 | 11 | 55 | 63 | 64 | 47 | 25 | 10 | 37 | 45 |
| $f_1$ ~cps | 39.4 | 47.6 | 47.6 | 40.0 | 36.1 | 44.9 | 54.8 | 38.2 | 32.6 | 42.6 | 44.7 | 44.7 | 41.6 | 40.8 | 40.8 | 45.6 | 52.6 |
| $f_2$ ~cps | 150.2 | 173.0 | 173.0 | 148.2 | 132.6 | 168.8 | 188.5 | 143.9 | 118.7 | 157.2 | 165.1 | 165.1 | 153.6 | 147.3 | 147.3 | 168.2 | 193.4 |
| $\omega_\phi/\omega_{h_1}$ | 1.525 | 2.67 | 2.67 | 2.67 | 1.585 | 1.53 | 2.64 | 1.500 | 0.90 | 2.080 | $\infty$ | $\infty$ | 1.486 | 0.90 | 0.90 | 1.500 | 2.67 |
| Mach No. | .890 | .997 | 1.030 | .792 | .760 | 1.175 | 1.087 | 1.052 | .803 | 1.050 | 1.062 | 1.001 | .920 | 1.053 | 1.190 | 1.178 | 1.178 |
| $V_E/b_r\omega_{h_1}\sqrt{\mu}$ | 1.712 | 1.839 | 1.854 | 1.788 | 1.743 | 1.782 | 1.768 | 1.570 | 1.665 | 1.499 | 1.828 | 1.796 | 1.682 | 1.468 | 1.130 | 1.573 | 1.685 |
| $\mu_E$ | 24.2 | 25.2 | 26.1 | 23.5 | 24.2 | 28.0 | 25.0 | 45.4 | 24.5 | 50.9 | 35.7 | 34.8 | 24.6 | 40.1 | 70.9 | 38.9 | 35.0 |
| f - cps | 95.0 | 94.7 | 92.3 | 87.4 | 89.7 | 103.0 | 100.0 | 74.0 | 96.9 | 69.9 | 84.0 | 83.8 | 87.4 | 77.3 | 62.1 | 84.1 | 88.9 |
| $P_o$ ~ lb/ft$^2$ | 2000 | 2100 | 2095 | 1925 | 1849 | 2300 | 2303 | 1021 | 1498 | 925 | 1372 | 1377 | 1623 | 1397 | 767 | 1523 | 1724 |
| Stag. Temp$_3$ °F | 111° | 117° | 118° | 75° | 95° | 138° | 123° | 84° | 72° | 99° | 115° | 116° | 86° | 114° | 81° | 126° | 135° |
| $\rho_E$ slugs/ft$^3$ | .001400 | .001341 | .001298 | .001560 | .001480 | .001210 | .001352 | .000664 | .001220 | .000587 | .000837 | .000882 | .001170 | .000796 | .000451 | .000821 | .000912 |
| $(\omega/\omega_\alpha)_E$ | .506 | .500 | .489 | .558 | .585 | .470 | .457 | .444 | .545 | .394 | .472 | .471 | .462 | .370 | .297 | .402 | .425 |
| $(V/b_r\omega_\alpha)_E$ | 2.280 | 2.542 | 2.603 | 2.393 | 2.422 | 2.547 | 2.352 | 2.930 | 2.193 | 2.845 | 2.901 | 2.820 | 2.295 | 2.475 | 2.542 | 2.614 | 2.660 |
| $V_E$ | 958 | 1077 | 1103 | 839 | 835 | 1250 | 1156 | 1093 | 872 | 1126 | 1155 | 1105 | 970 | 1157 | 1191 | 1226 | 1247 |
| $V_E/V_R$ | 1.112 | 1.182 | 1.209 | 1.134 | 1.181 | 1.179 | 1.094 | 1.114 | 1.108 | 1.017 | 1.138 | 1.107 | 1.120 | 1.036 | .901 | 1.054 | 1.064 |

E = Experimental Data
R = Reference Analysis

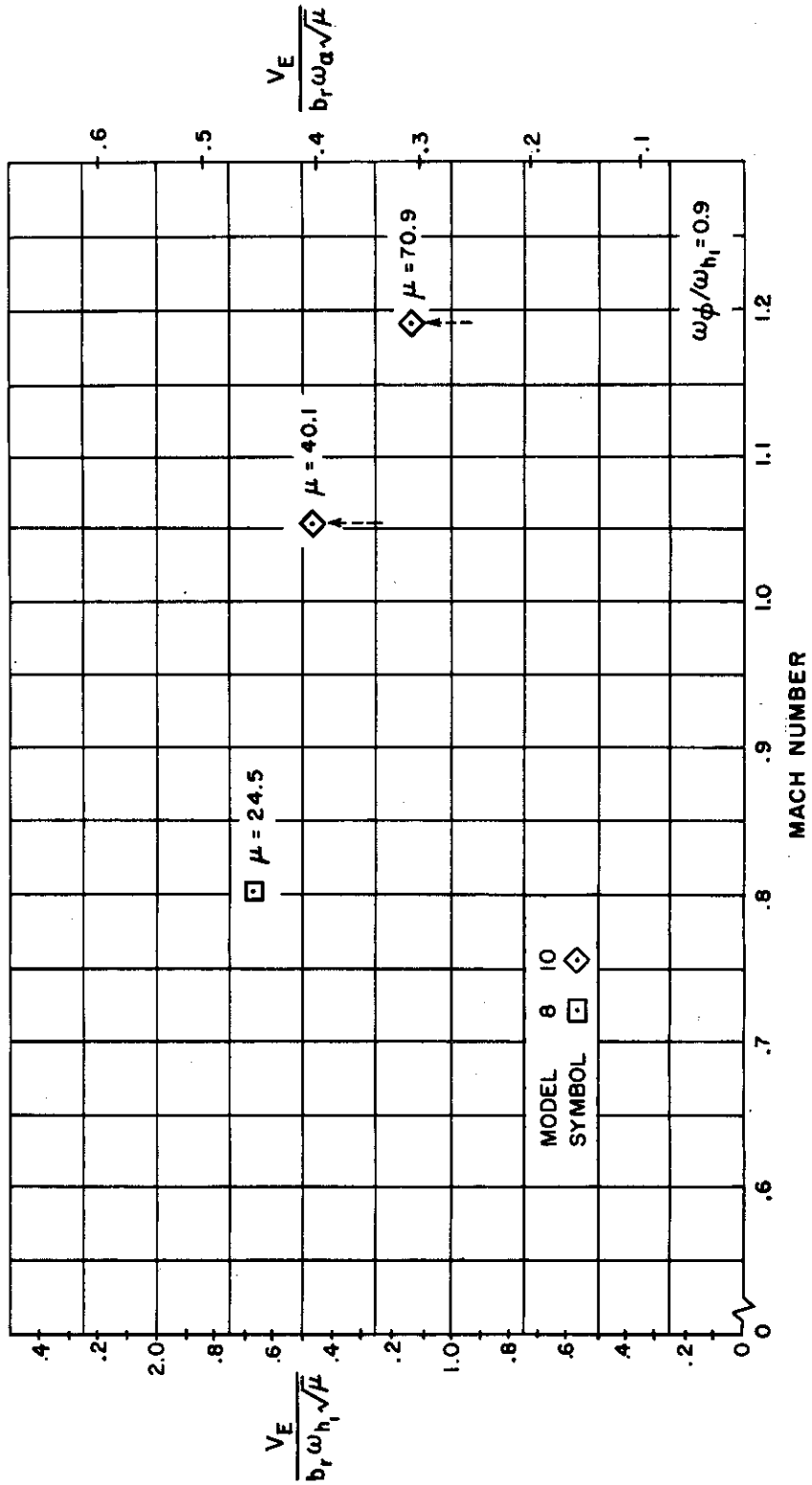


Figure 7. Reduced velocity versus Mach number for pitch to bending frequency ratio of 0.9. Numbers beside data points indicate mass ratio at flutter. No faired curve has been drawn due to the wide variation in mass ratio between test points. Dotted arrows indicate path followed in approaching flutter.

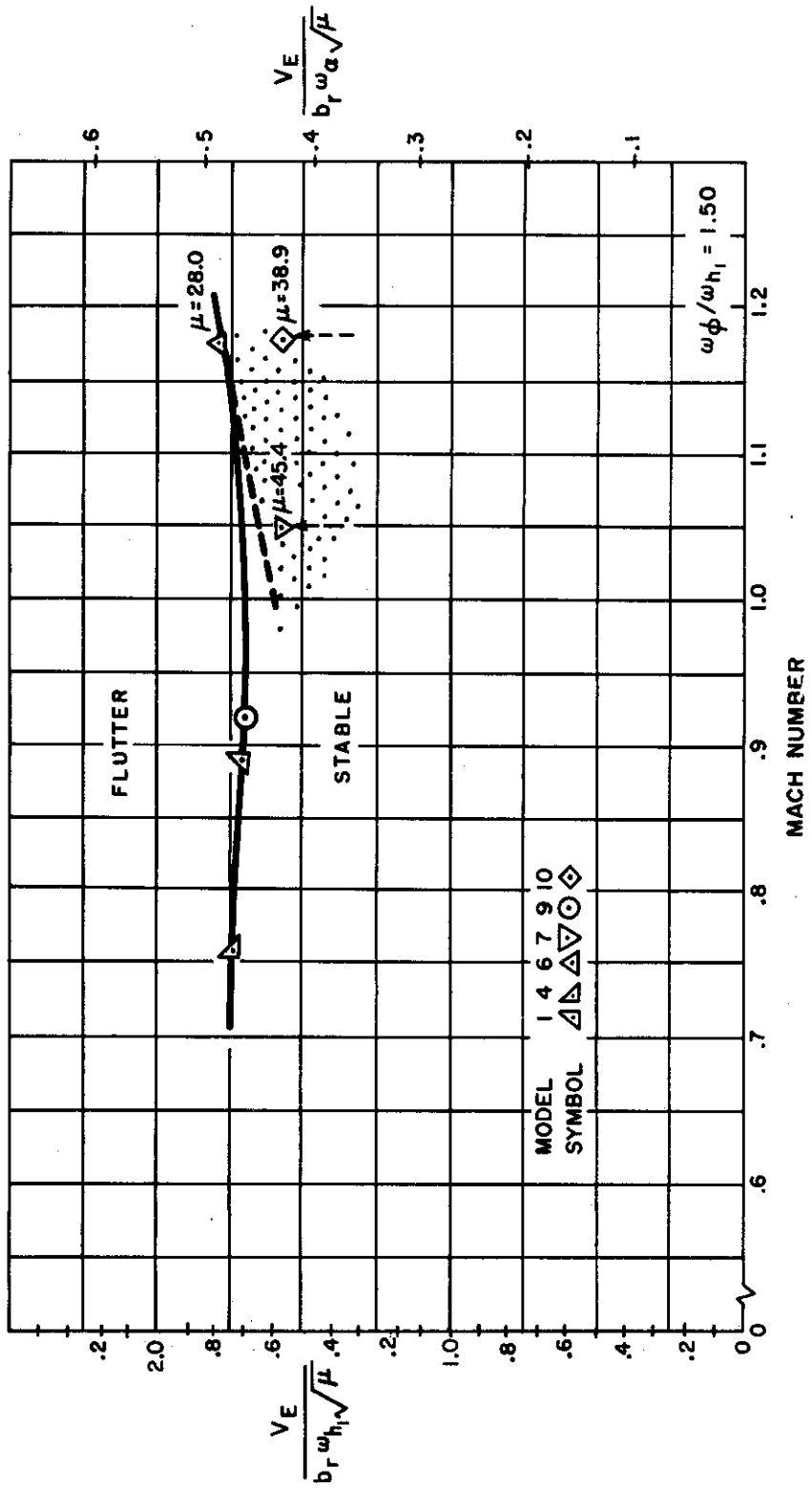


Figure 8. $V_E/b_r\omega_{h_1}\sqrt{\mu}$ versus Mach number for $\omega\phi/\omega_{h_1} = 1.5$, $\mu$ = 25 except where noted. Dotted area indicates low flutter stability. Phantom line is $\mu$ = 25 path followed in getting flutter with model 6 at Mach 1.17. The $\mu$ = 25 flutter boundary must pass above the phantom line for lower Mach numbers indicating a negligible "transonic dip".

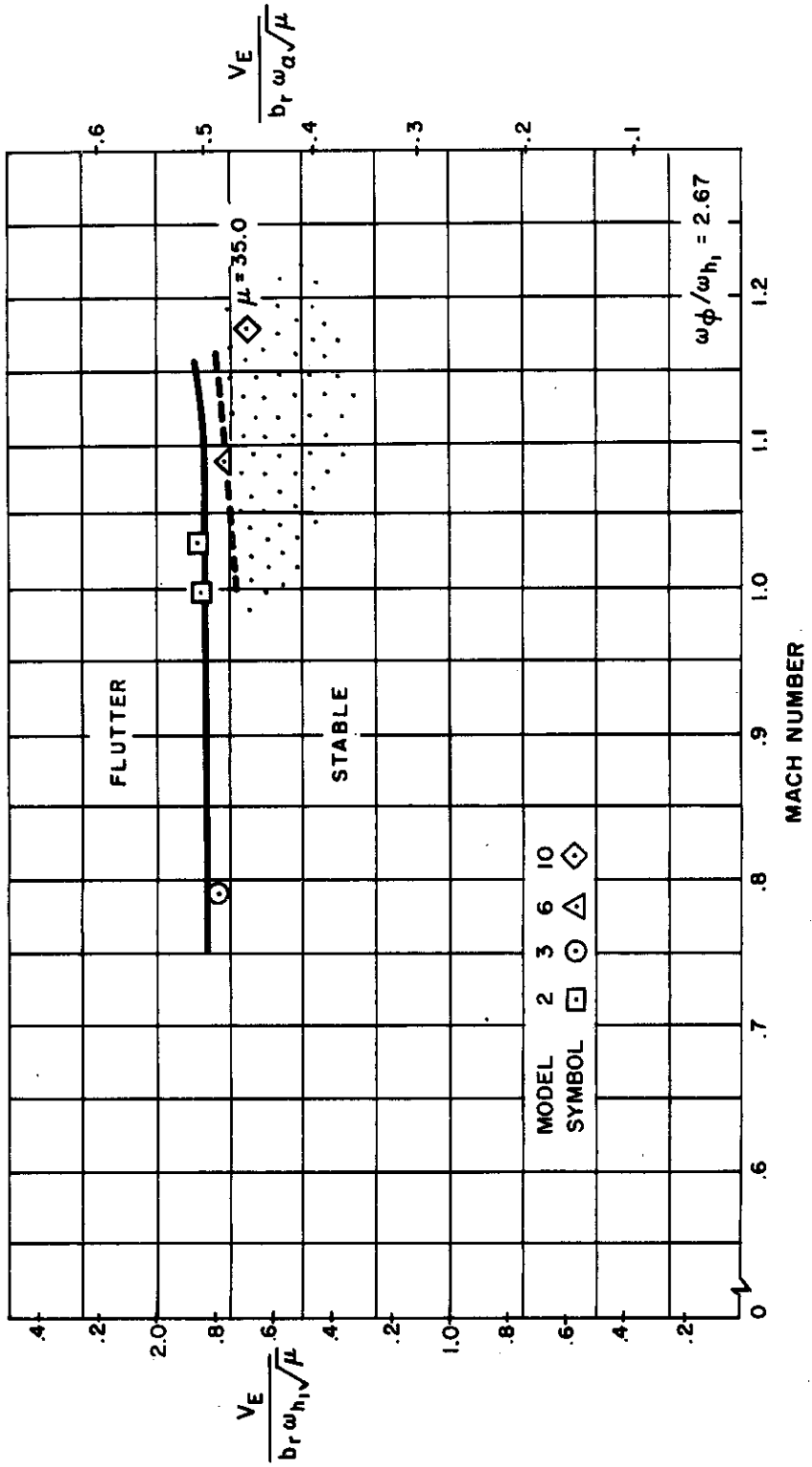


Figure 9. $V_E / b_r \omega_{h_1} \sqrt{\mu}$ versus Mach number for $\omega_\phi / \omega_{h_1} = 2.67$ and $\mu = 25$ except as noted. Model 6 traced out the phantom line at $\mu = 25$ with a marginal flutter condition at Mach 1.09. The $\mu = 25$ flutter boundary, therefore, passes above this phantom line indicating a negligible "transonic dip". Dots indicate low stability area.

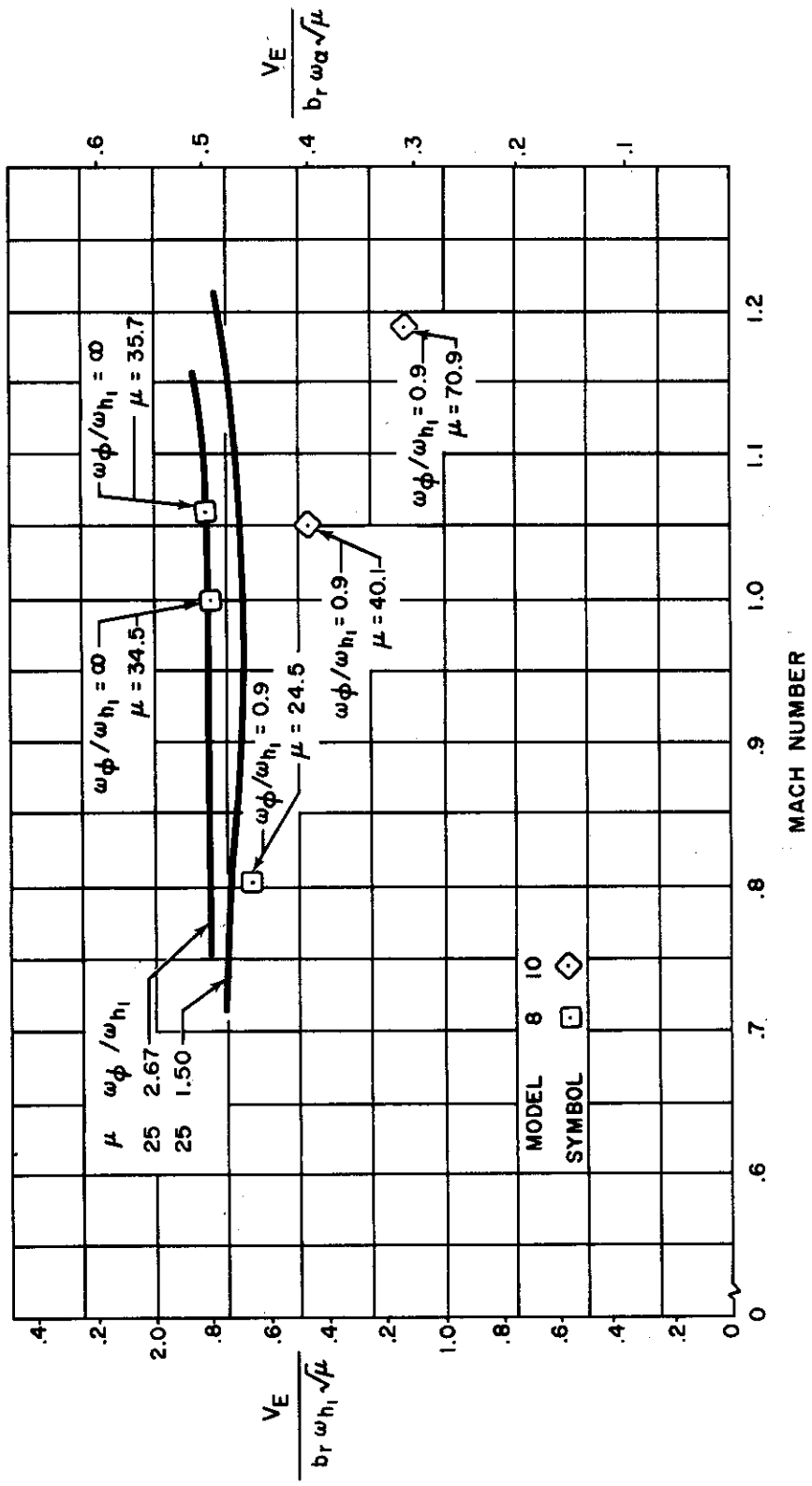


Figure 10. $V_E/b_r\omega_{h_1}\sqrt{\mu}$ versus Mach number showing the $\mu$ = 25 trend lines taken from Figures 8 and 9 for $\omega_\phi/\omega_{h_1}$ = 1.50 and 2.67. Data points at $\omega_\phi/\omega_{h_1} = \infty$ and 0.9 are also shown.

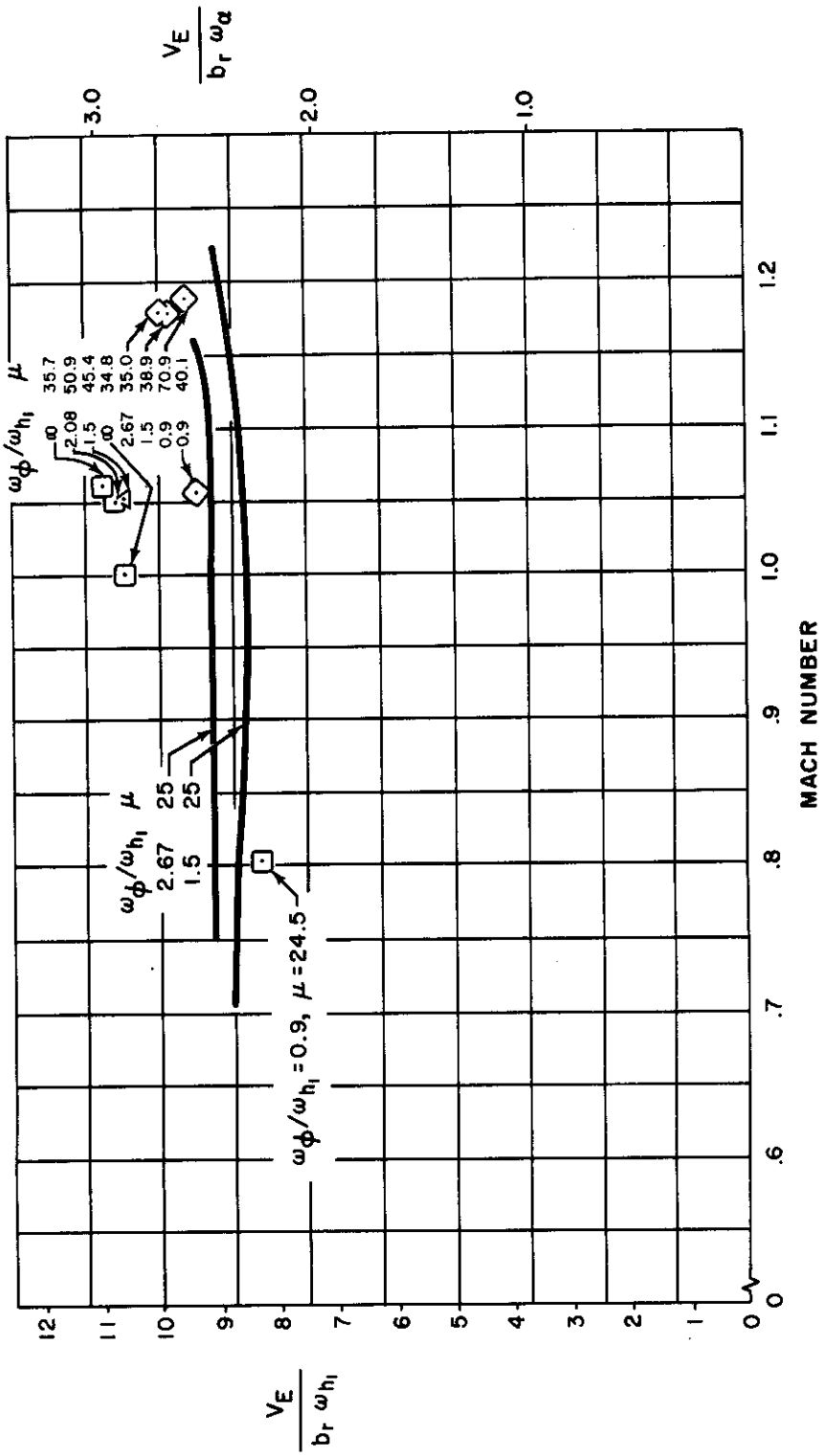


Figure 11. Reduced velocity versus Mach number for $\omega\phi/\omega_{h_1}$ = 0.9, 1.5, 2.67 and $\infty$ . The $\omega\phi/\omega_{h_1}$ = 2.67 and 1.5 data is represented by $\mu$ = 25 trend curves obtained from the faired curves of Figures 8 and 9, respectively.

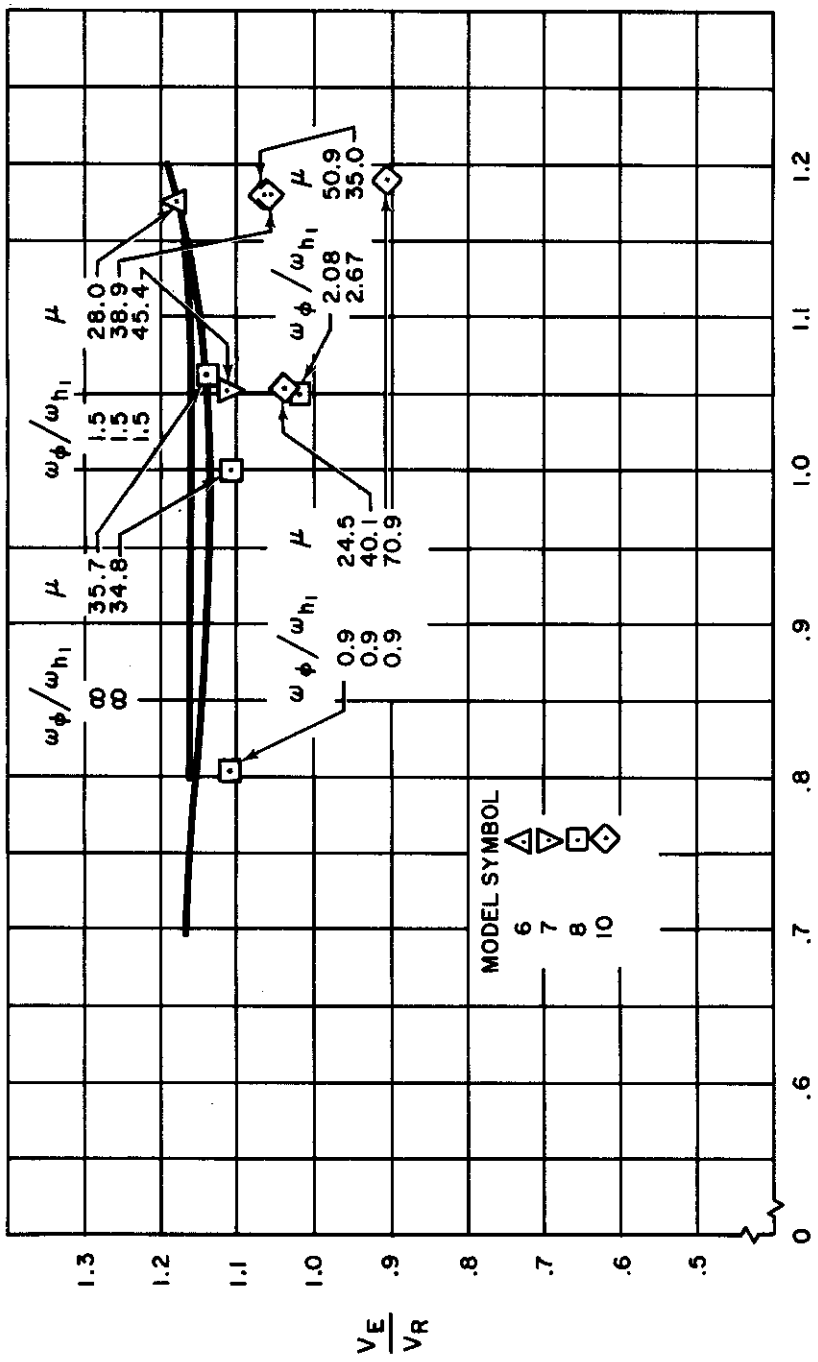


Figure 12. $V_E/V_R$ versus Mach number. The decreased margin of conservatism of incompressible analysis with mass ratios above 25 in the transonic speed range is clearly illustrated. Data at $\mu = 25$ is indicated by the solid lines. Data at higher mass ratios are represented by the individual data points.

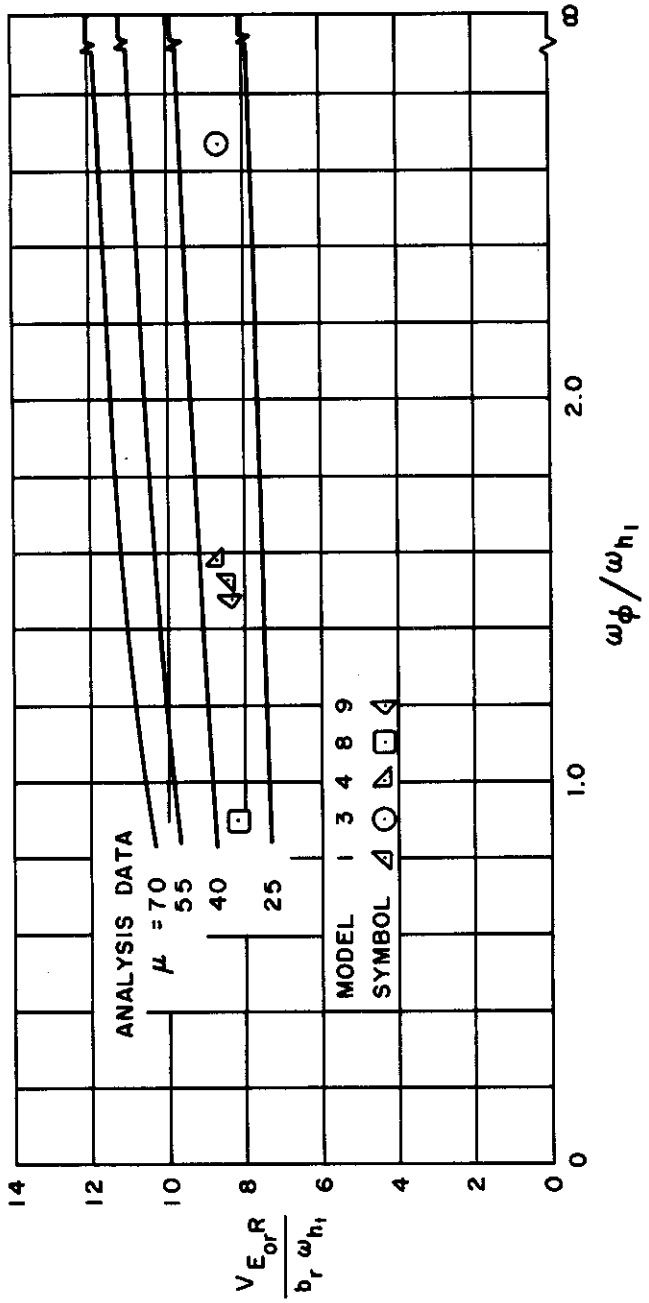


Figure 13. Test Data for $M \leqq 0.92$ to show subsonic trend of $V_E$ $b_r \omega_{h_1}$ versus $\omega_\phi / \omega_{h_1}$. Mass ratios of points shown range between 23.5 and 24.6. Reference analysis data is included for comparison.

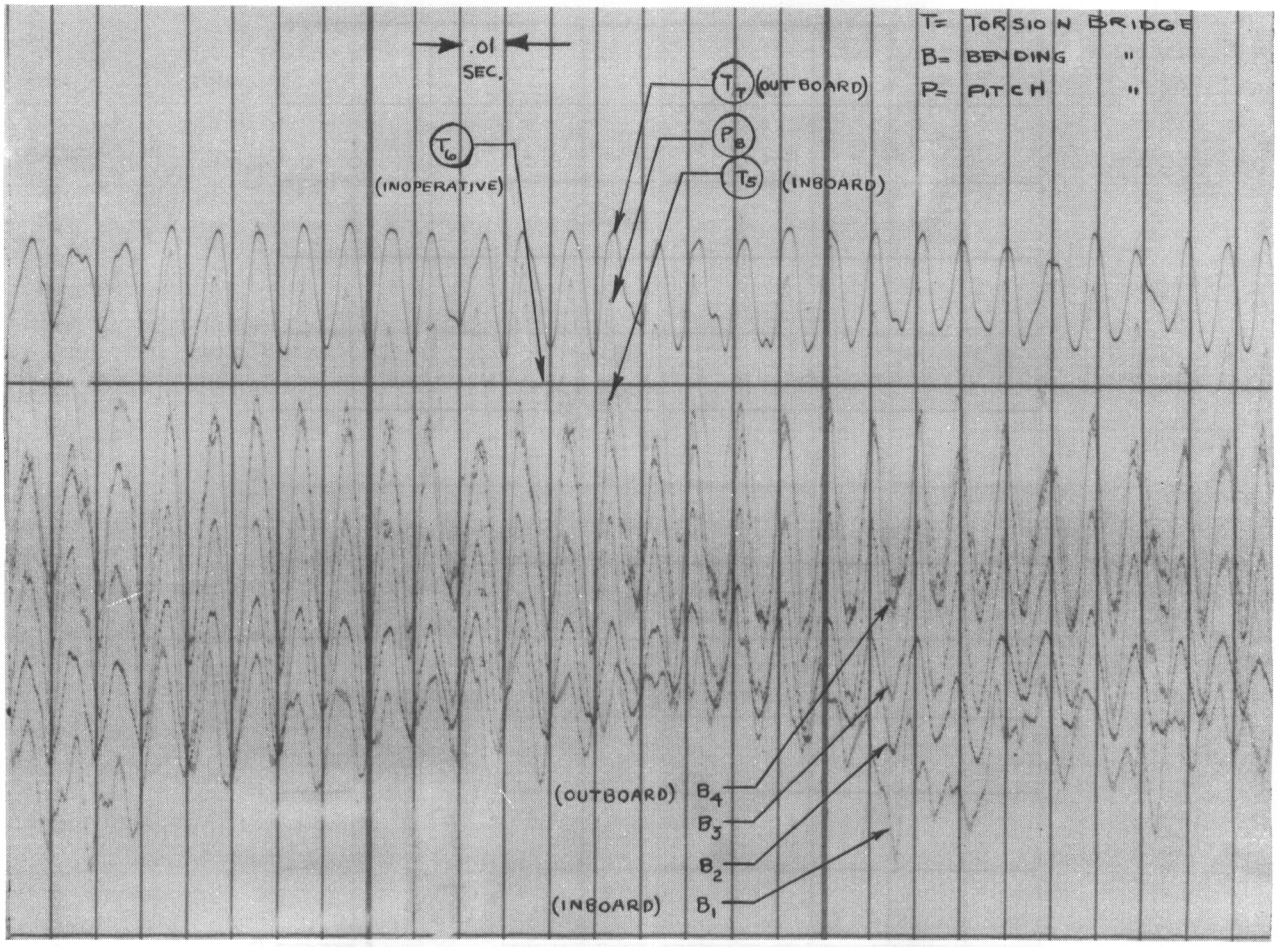


Figure 14. Oscillograph record of flutter of model 6. Test point 115 of first test period. $\omega_\phi/\omega_{h_1}$ = 1.53, Mach 1.175, $\mu$ = 28.0. Model diverged in flutter about ten second after record was taken.

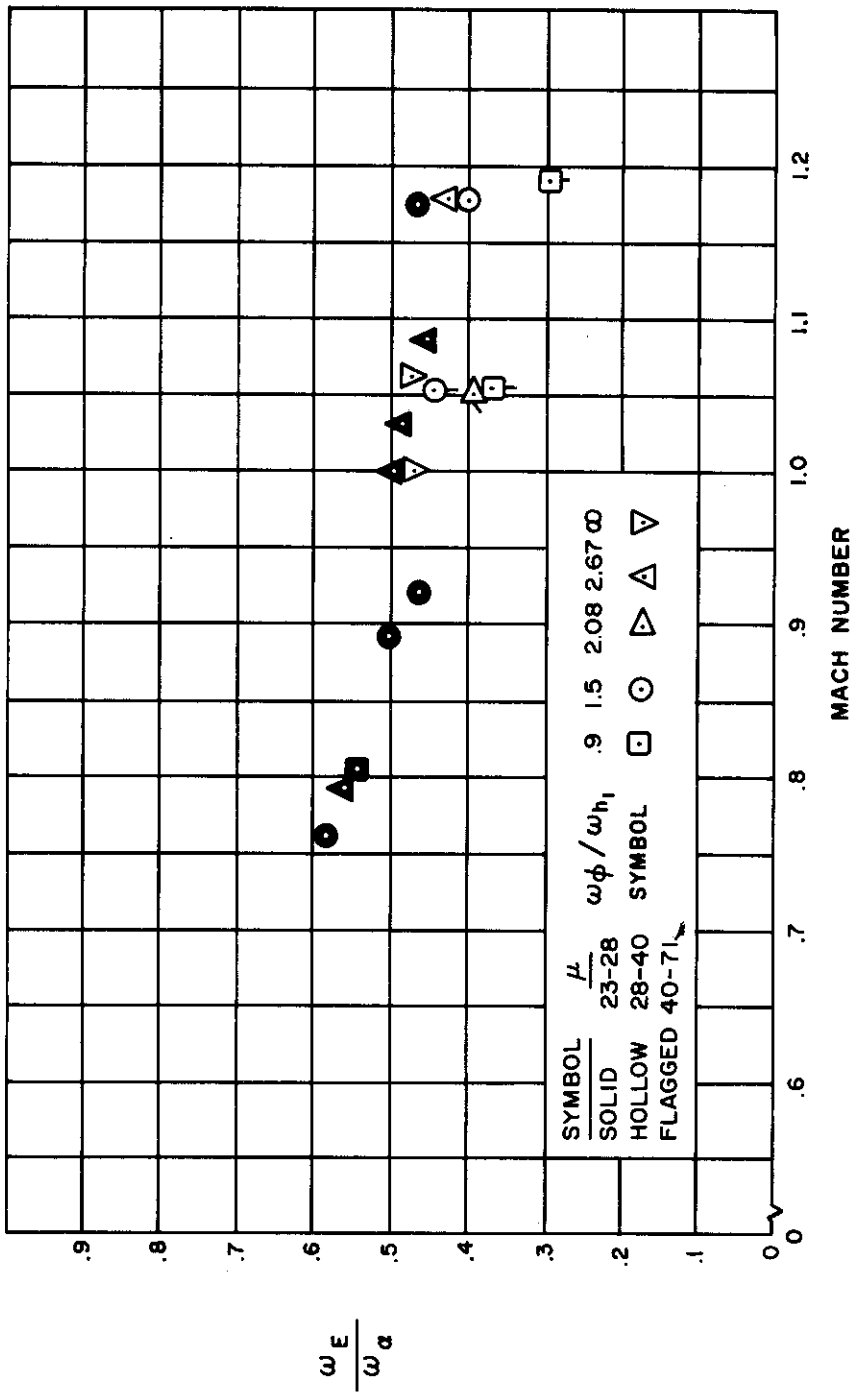


Figure 15. Experimental flutter to torsion frequency ratio versus Mach number.

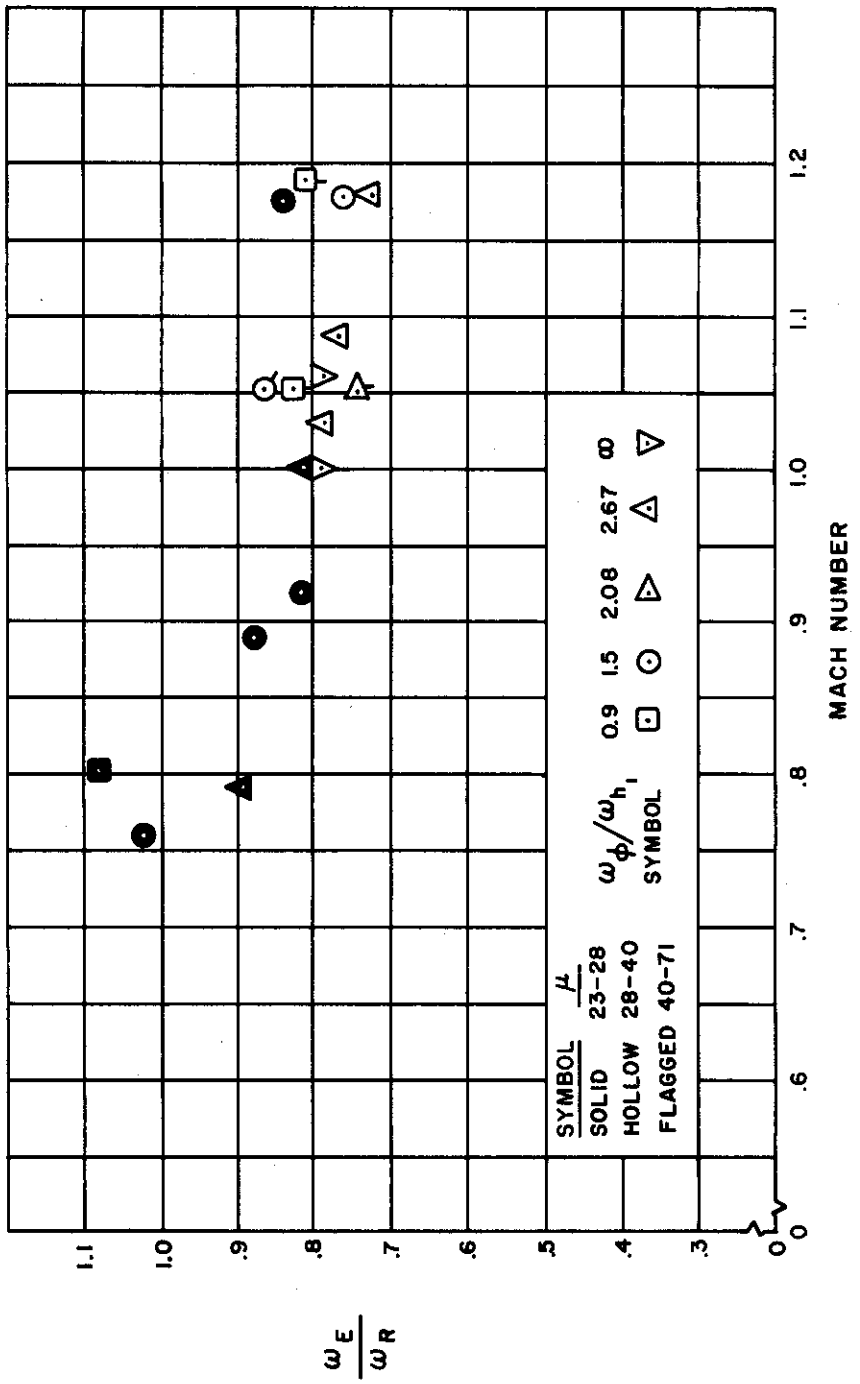


Figure 16. Ratio of experimental to analysis flutter frequencies.

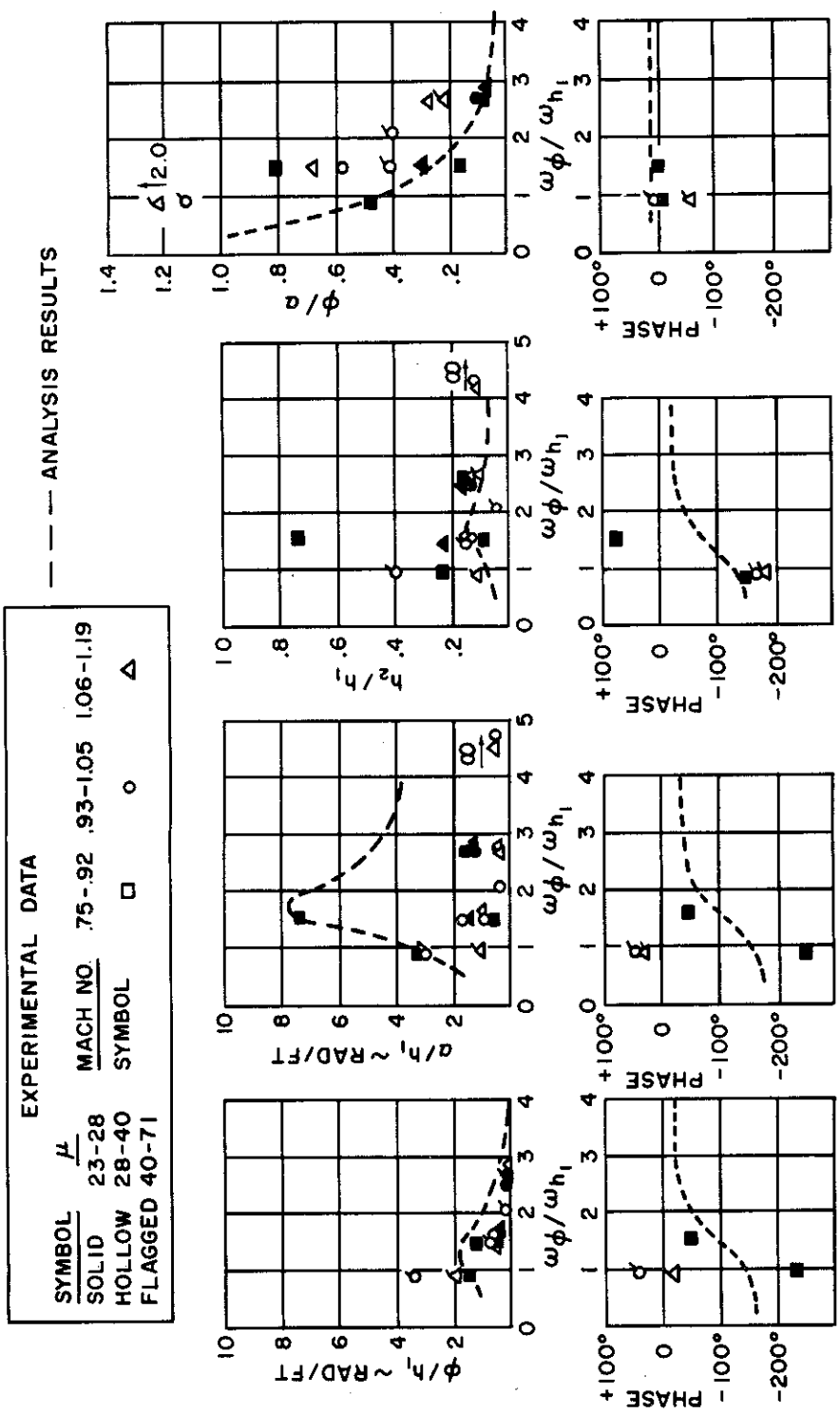


Figure 17. Experimental and Analytical Amplitude Ratios and Phase Angles versus Pitch to Bending Frequency Ratio.

## SECTION 4

## CONCLUSIONS

1. For a mass ratio of 25 and pitch to bending frequency ratios $\omega_\phi/\omega_{h_1}$ of 1.5 and 2.67 the stabilizer configuration of this program showed a negligible sensitivity to compressibility effects having neither a pronounced transonic dip nor supersonic rise. For $\omega_\phi/\omega_{h_1}$ =2.67, $V_E/b_r\,\omega_{h_1}\sqrt{\mu}$ remained between 1.74 and 1.80, while for $\omega_\phi/\omega_{h_1}$ =1.5 this parameter remained between 1.64 and 1.74 for test Mach numbers between 0.75 and 1.19. For all of the above test conditions the ratio of observed flutter speed to analytically predicted flutter speed remained between 1.13 and 1.19.

2. The conservatism of reference analysis appears to decrease as mass ratio is increased above 25. The extreme case occureed at M 1.19, $\omega_\phi/\omega_{h_1}$ = 0.9 and $\mu$ = 70.9 where the analysis gave a flutter velocity 10% below the experimental value. It appears that this loss of conservatism is due to the relatively small increase in flutter speed brought about experimentally by increasing $\mu$ as compared to reference analysis predictions. However, further data are required to definitely establish that compressibility and pitch to bending frequency ratio are not significant in this connection.

3. The effects of variations in pitch to bending frequency ratio with mass ratio constant at 25.0 are small and of the same order of magnitude as are predicted by reference analysis. Data points below Mach 0.92 at $\mu$ = 25, show a drop of 5% in $V_E/b_r\,\omega_{h_1}$ as $\omega_\phi/\omega_{h_1}$ drops from 2.67 to 0.9. Analyses show a corresponding drop of 6%. The drop in $V_E/b_r\,\omega_{h_1}$ in going from $\omega_\phi/\omega_{h_1}$ = 2.67 to 1.50 does not exceed 7% at any point between Mach 0.8 and 1.15 at $\mu$ = 25.0.

4. A region of low stability most prominent at Mach numbers greater than 1.0 exists beneath the flutter boundary at all pitch to bending frequency ratios.

5. Observed flutter frequencies were close to analyses frequencies in the vicinity of Mach 0.75. Increasing Mach number from 0.75 to 1.2, at $\mu$ = 25 resulted in a drop in $\omega_E/\omega_\alpha$ of about 20%, indicating increased prominence of the first bending mode in the flutter mode.

6. Both experiment and analysis show that for the pitch axis location used the pitch degree of freedom does not become significant amplitude-wise until $\omega_\phi/\omega_{h_1}$ drops down close to unity. Analyses show that the first bending mode shifts from a roughly in phase conditions with pitch at $\omega_\phi/\omega_{h_1}$ = 2.5 to a roughly out of phase condition for $\omega_\phi/\omega_{h_1}$ = 1.0. This was only roughly confirmed by experiment.

[redacted]

## SECTION 5

## RECOMMENDATIONS

1. The models of this program were designed to give flutter information in the Mach 0.8 to 1.2 range at $\mu = 25$ and $1.5 < \omega_\phi/\omega_{h_1} < 4.0$. At the time of testing, interest had broadened to include $\omega_\phi/\omega_{h_1}$ down to 0.9 plus the effects of increases in $\mu$. The very limited number of flutter points which could be obtained per model prevented complete coverage of the ranges of variables varying only one parameter at a time to allow a determination of the separate effects of each. It is therefore recommended that additional models of the present configuration be tested at $\mu = 25$ for $\omega_\phi/\omega_{h_1} = 0.9$ and $\infty$ for the Mach 0.8 to 1.2 range to complete the parameter study at $\mu = 25$. A repetition of much of the $\mu = 25$ program at $\mu = 45$ and 70 would be desirable to study the effects of mass ratio variations particularly at $\omega_\phi/\omega_{h_1} = 0.9$ where reference analyses apparently become unconservative.

2. In view of the important effect of pitch axis location on the influence of the pitch degree of freedom on flutter speed which has been demonstrated by WADC tests at subsonic speeds, it is recommended that tests be performed with pitch axis as a variable to allow the effect of this parameter to be established at transonic speeds. In view of the many cases of all movable stabilizer flutter which have occured in recent years, it would also be desirable to run additional tests covering variations in aspect ratio, taper ratio and sweep to allow the designer to avoid critical combinations of flutter parameters.

3. The measurement of amplitude ratios and phase angles during flutter is a difficult, costly and time-consuming operation of limited accuracy when done in terms of instrumentation attached to the model. It is recommended that in future programs high speed photographic facilities (2,000 to 8,000 frames/second) be developed to supplement other methods in the study of flutter modes and general model performance. At the present time camera location, loading, triggering, and lighting problems usually reduce the practicability of high speed photography.

4. The present program illustrates the need for wind tunnels more suited to flutter testing. Desirable features of such a tunnel would be: (1) blowdown rather than continuous flow type (or other devices) to allow higher test densities (1-2 atmospheres) to avoid the danger of fan blade damage and to reduce flow turbulence; (2) many access doors and windows to allow maximum flexibility in model mounting or injection, model clamping, and photgraphing (up to 8,000 frames/second) with adequate lighting.



[redacted]

## BIBLIOGRAPHY

1. Barmby, J. G., Cunningham, H. J., and Garrick, I. E., Study of Effects of Sweep on the Flutter of Cantilever Wings. NACA Report 1014. National Advisory Committee for Aeronautics, 1951.

2. D'Ewart, Benjamin B., and Ryken, John M., (UNCLASSIFIED TITLE) Cantilever Wing Flutter Model Tests At Low and Transonic Speeds. WADC Technical Report 53-47. Wright Air Development Center, Wright-Patterson Air Force Base, Ohio, November 1954. (CONFIDENTIAL REPORT)

3. Maier, Henry G., and King, Stephen R., (UNCLASSIFIED TITLE) Transonic Flutter Model Tests, Part I. 45 Degree Swept Wings. WADC Technical Report 56-214, Part I. Wright Air Development Center, Wright-Patterson Air Force Base, Ohio, September 1957. (CONDIDENTIAL REPORT).

# APPENDIX I

## Model Details

### 1. Geometry and Dimensions

A sketch, brief description of the test configuration and summary of basic characteristics is given in Section 1. Additional dimensions which may be useful for reference purposes have been included in Figure 18. Dimensions shown are common to each of the 10 models tested. It was originally intended that the elastic axes of the models run along the 40% chord line. Factors of unknown origin, however, caused a rearward shift resulting in an average EA location of 41.6% chord.

### 2. Stabilizer Construction

The models were of single beam stressed skin construction with solid styrofoam core used for skin stabilization. Beam width and skin thickness dimensions were adjusted from model to model to obtain the desired range of frequencies. The construction is shown in Figures 19 and 20. The main beam was formed from 75 ST aluminum alloy sheet bent into two channel sections and riveted back to back. Sheet thickness was tapered to obtain proper mass and elastic variations down the span. The I-beam was riveted and bonded to a steel root fitting between stations 2.9 and 3.6. The intersection of the elastic axis with the fuselage surface is designated station 0. To provide chordwise stiffness 0.020 inch aluminum ribs were spaced at 2.9 inch intervals down the span. For Models 1, 2, 5 and 6 which were tested first, flat ribs were used. For the remaining models the ribs were flanged top and bottom to provide greater rib stiffness and area for bonding ribs to the structural skin.

It was found that the skin buckling loads could be more than doubled by the addition of light stringers. These were formed by bending 0.004 inch sheet aluminum into angles 0.06 wide and 0.10 deep. These were bonded to the styrofoam flush with the surface in the heavily stressed portions of the stabilizer. Ballast was added ahead of and behind the main beam as required to control the c.g. and mass moment of inertia of each model.

The skin was 75ST6 sheet ground to the required thickness and taper to provide the desired contribution to bending and torsion stiffness for each model. The sheet was bent with a .016 radius (hot formed) around the leading edge and bonded closed along a trailing edge seam. The skin was bonded to the internal structure using carefully controlled quantities of bonding resin to obtain a satisfactory bond while maintaining accurate control over mass characteristics. To allow transfer of skin loads into the steel root fitting, the beam-root fitting joint between stations 2.9 and 3.6 was contoured flush with the skin and extended in the chordwise direction as indicated in Figure 19 to provide a large bond area for the skin. The steel root fitting mass was kept closely centered about the pitch axis to avoid excessive pitching moment from this source.

Bending moment sensitive strain gage bridges were located at stations 1.2 and 11.5. The inboard bridge was mounted to the steel root fitting while the outboard bridge was bonded to the inside of the stabilizer skin for maximum sensitivity. A torque sensitive strain gage bridge was placed on the steel root fitting at station 1.9.

The relatively intricate construction used for these models was considered most practical to meet the $\mu = 25$ requirement at the low tunnel densities required for supersonic speed, and at the same time build sufficient strength into the models to allow them to resist hours of exposure to low stability and high turbulence conditions during the probing for flutter boundaries.

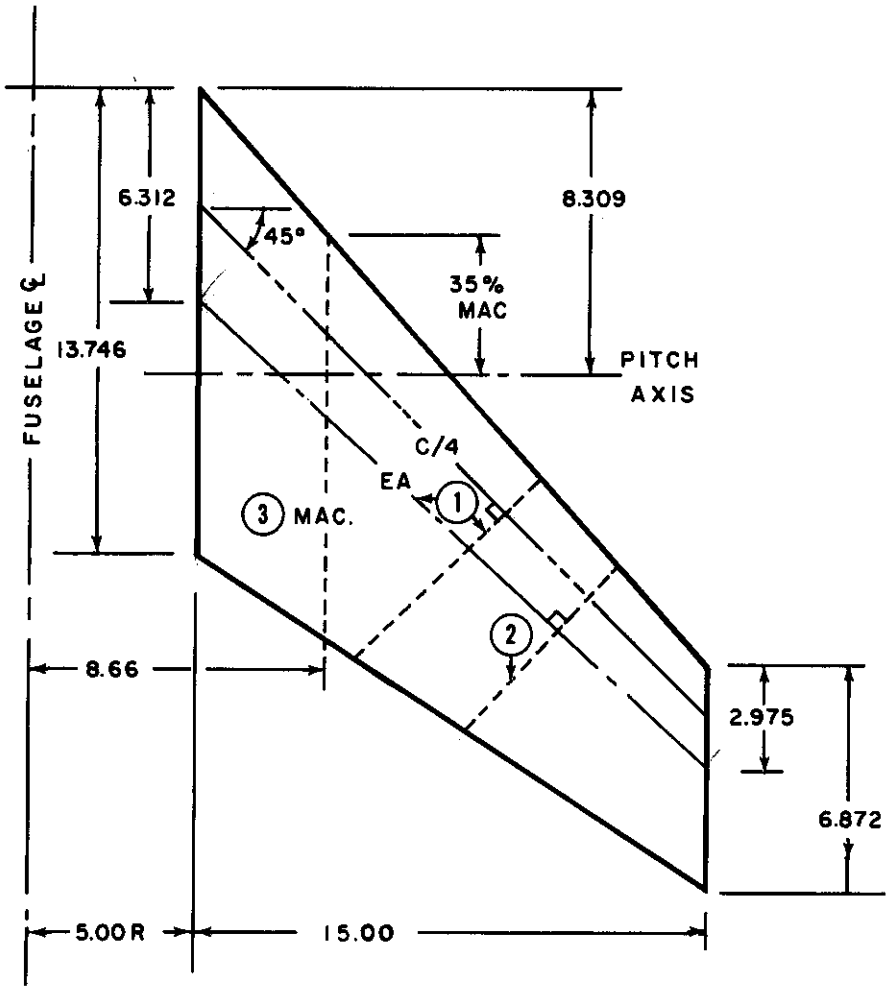


(1) E.A. located at 41.6% chord measured along chord perpendicular to quarter chord.

(2) c.g., $x_\alpha$ and $r_\alpha^2$ taken in direction of chord perpendicular to elastic axis. See table 1.1 for specific values.

(3) MAC based on span to center of fuselage = 12.07"

(4) C/4 Taken in Windstream Direction.

Figure 18. Stabilizer Model Dimensions and Geometry

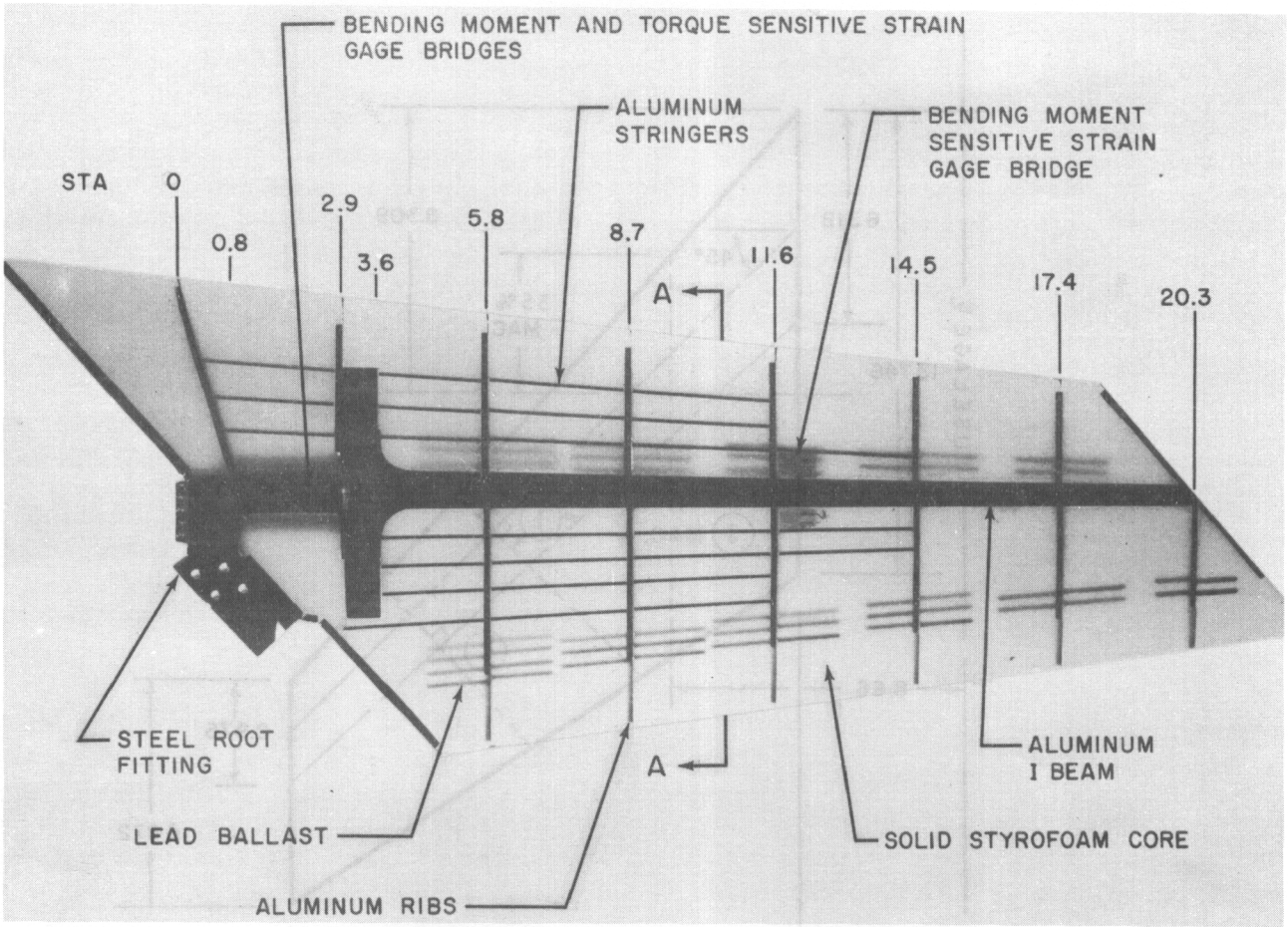


Figure 19. Typical stabilizer before aluminum skin was bonded in place. Photograph obtained with rear lighting showing internal ballast and other parts against translucent styrofoam core.

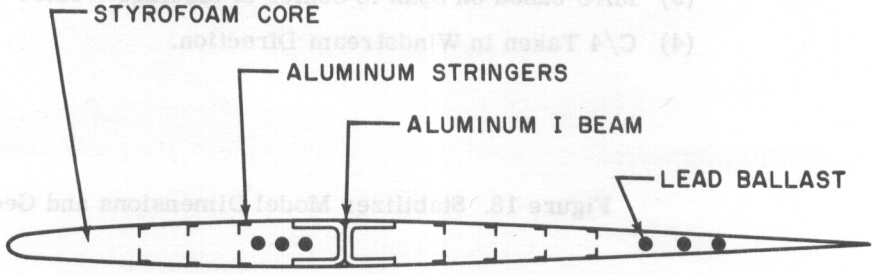


Figure 20. Crossection of Stabilizer indicated in Figure 19

3. Model Mount Characteristics

Figure 21 shows the complete test assembly mounted in a jig for laboratory tests. The fuselage was of wood with the center section hollowed out to provide space for model control mechanisms as shown in Figure 22. An aluminum cover plate was used to close this section. A sponge rubber seal between fuselage and stabilizer was provided for the first four models tested. This was replaced by a close clearance contoured block (not shown) for the tests of the remaining models. Pitch excitation was provided by an electromagnetic shaker applying an oscillating force tangent to the surface of the torque tube. The lower solenoid shown in Figure 22 was connected to a linkage which locked out the pitch degree of freedom. The upper solenoid was connected to a brakeshoe type damping device.

The mechanism for controlling pitch frequency is shown in the rear view of the assembly as presented in Figure 23. A long steel spring was attached to the end of the stabilizer torque tube. The carriage, which can be driven the length of the spring, clamps the spring rigidly by means of a preloading device to prevent any free play or binding due to variations in spring thickness. The carriage track rollers are preloaded against the track for the same purpose. Position of the carriage was indicated through a revolution counter connected to the carriage drive system.

The stabilizer torque tube was mounted on flexure pivots to avoid the inertia and friction of bearings. Strain gages attached to these flexure pivots provided pitch displacement information.

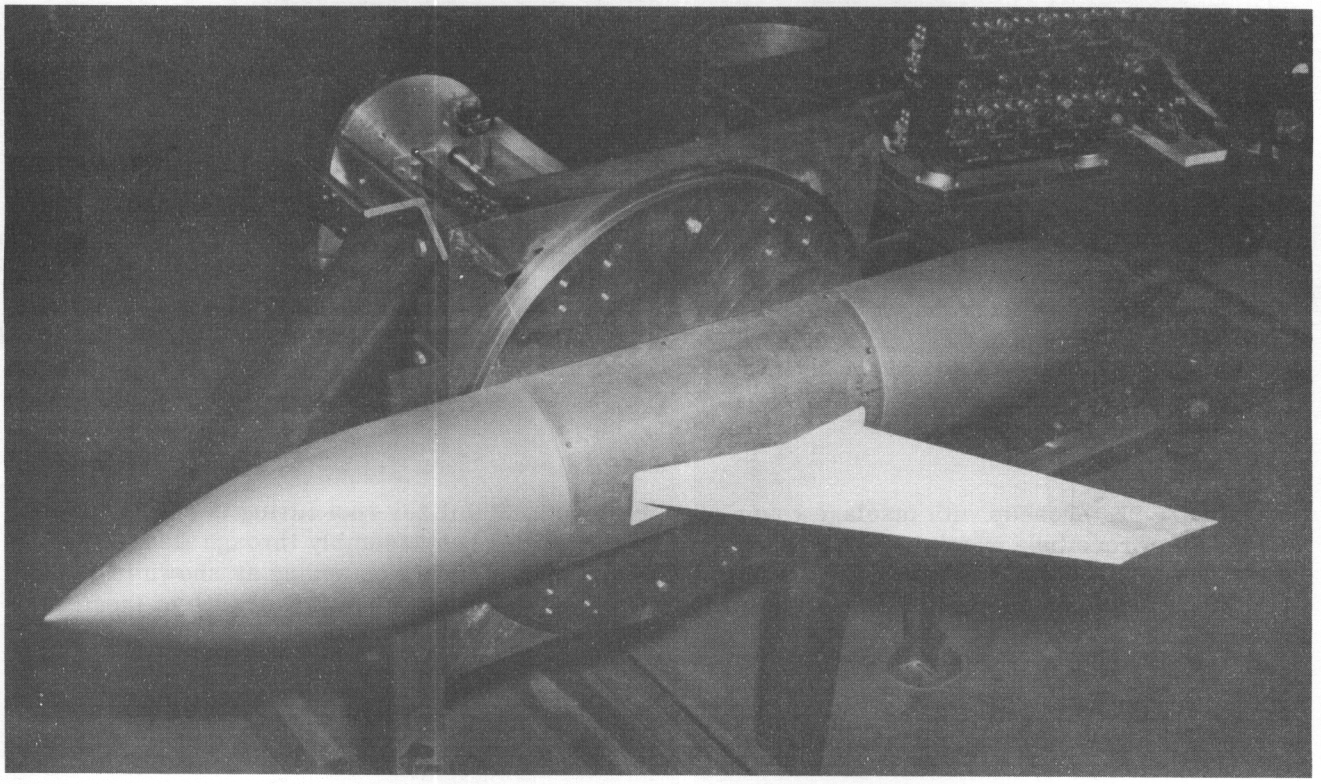

Figure 21. Test assembly mounted in laboratory fixture. The circular steel plate to which the fuselage is attached is installed in a tunnel wall window opening.

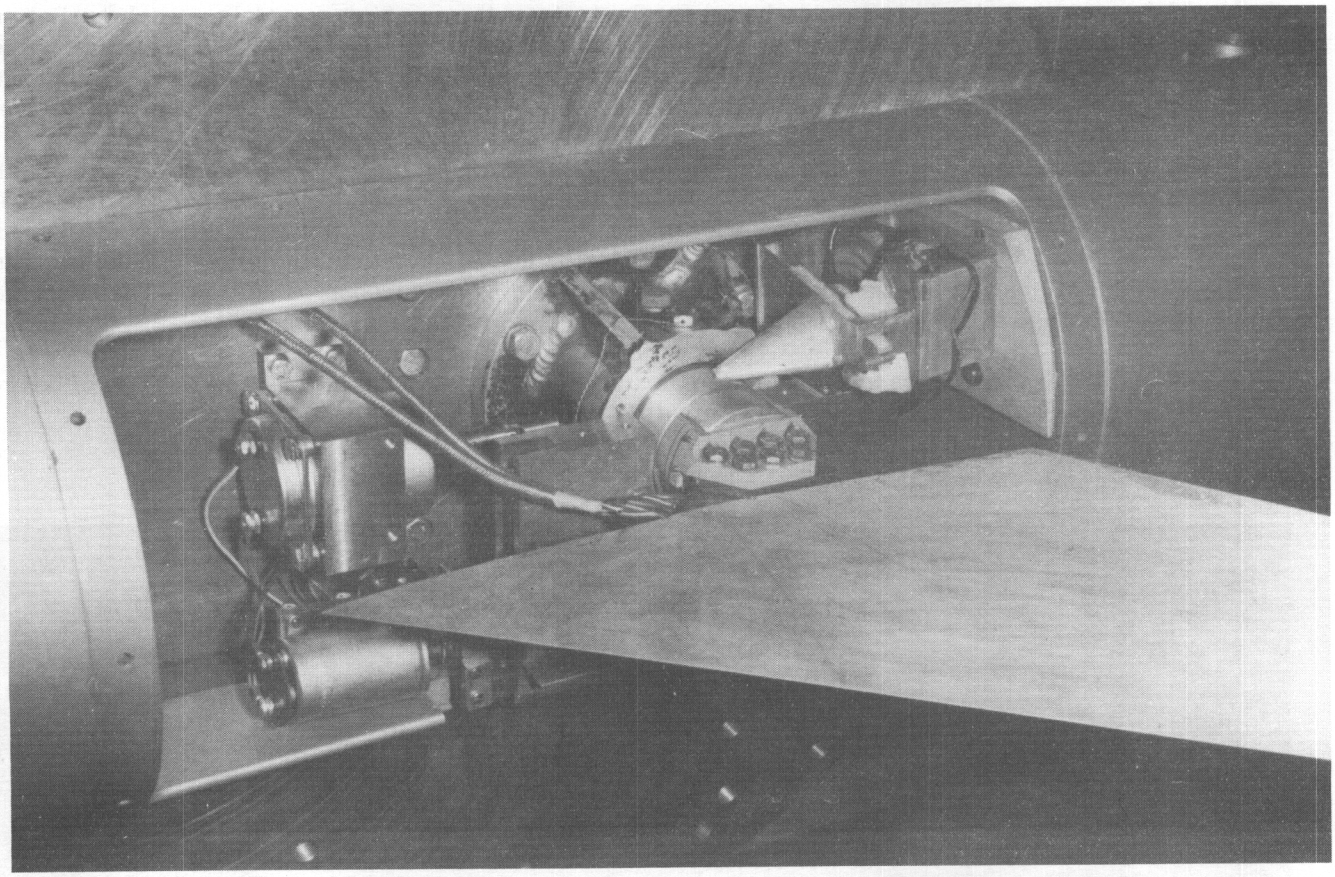

Figure 22. Closeup with fuselage cover plate removed. Stabilizer root fitting is shown bolted to the torque tube which in turn is supported by the welded hub assembly through flexure pivots. The torque tube extends through the wall and is attached to a torsion spring as shown in Figure 23. The solenoids at the left operate mechanisms for locking out the pitch degree of freedom.

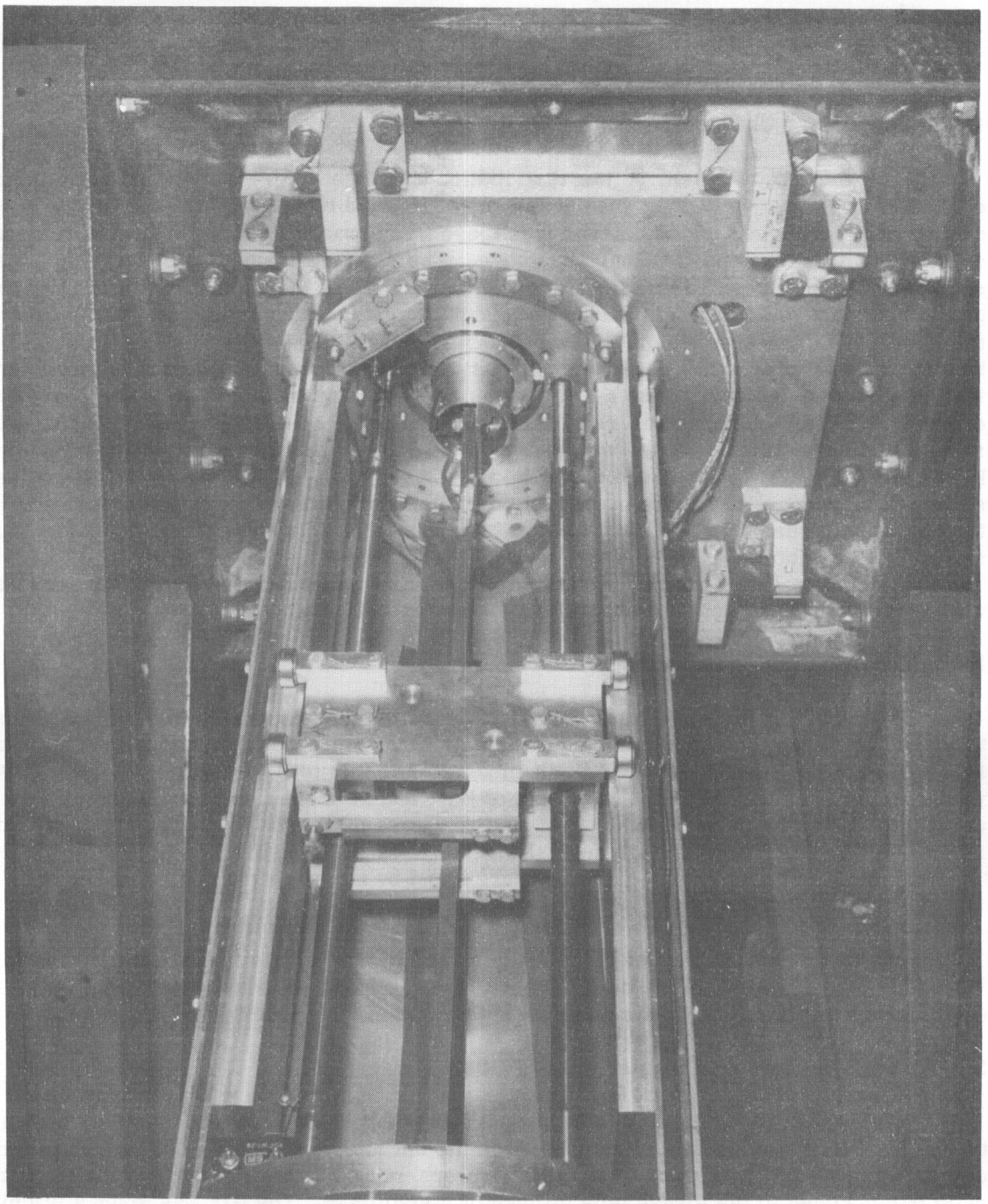

Figure 23. View of pitch restraint system behind tunnel wall. The pitch restraint spring is in a vertical plane with one end attached to the stabilizer torque tube. The effective length of the torque tube is controlled by the position of the carriage which clamps the spring firmly while traveling along its track driven by the two screw drive shafts.

## APPENDIX II

## MODEL CHECKS AND CALIBRATIONS

### 1. Model Mass Characteristics

A direct measurement of the distribution of weight, c.g. location and mass moment of inertia could not be made by slicing the models up after wind tunnel testing as all models were destroyed during test. However, close control over these items was maintained by measurement of the weight of each component prior to final assembly. The proper amount of ballast at each station was then computed and incorporated into the models. An estimate of the bonding resin used to bond the skin in place was made and taken into account in computing ballast requirements. Final weight and $I_\alpha$ distributions were corrected for the actual amount of bonding resin used by assuming that the difference between actual weight and design weight was due to a uniform layer of bonding resin over the entire inner surface of the skin. (The method of application assured this.) This procedure left a minimum chance for error and provides reasonable assurance that the design values of c.g. = 50% chord and $r_\alpha^2 = 0.25$ were met. Model weight, $I_\alpha$ and $x_\alpha$ over the span are given for each model in Table III. The values of $x_\alpha$ are based on a c.g. at 50% chord and elastic axes positions determined as described in Appendix II 2. Mass characteristics for the non-uniform station-widths at the root and tip were established allowing for the cutouts due to sweep in those regions. Models 1, 2, 5 and 6 were ballasted to maintain $\mu = 25.0$ down the span for a tunnel test section density of 0.001352 slugs/ft$^3$. The remaining models were made somewhat lighter by using the minimum ballast for each model that would give the proper non-dimensional mass characteristics.

### 2. Model Elastic Characteristics

The aspect ratio and chordwise stiffness of the models were sufficiently high to allow simple beam theory to apply. Model EI and GJ distributions and elastic axis locations were determined by load deflection measurements for each model. For this test the models were cantilevered. Loads were applied at station 17.4 on the 40% chord line, and 10 inches forward and aft of this point. Vertical translations and rotations of inboard stations were measured by pairs of dial indicators as shown in Figure 24. Dial indicator incremental loading effects were investigated and found to be negligible. The EI and GJ distributions of Table III were found by adjusting the design values until computed deflection shapes matched the experimental data.

Table I in Section 1 gives the average value of elastic axis location determind for each model. Since the c.g. has been taken at 50% chord for all models the elastic axis position down the span of each model may also be seen from the $x_\alpha$ distributions given in Table III.

### 3. Mass and Elastic Characteristics of Pitch System

To allow any desired pitch to bending frequency ratio to be realized during laboratory and wind tunnel testing it was necessary to determine the uncoupled pitch frequency which would occur at any carriage position. Laboratory calibrations were run on both pitch springs for this purpose using a rigid bar mounted to the torque tube in place of a stabilizer. The bar was given a pitching moment of inertia of 21.27 lb. in.$^2$ so that it simulated an average model. Calibration curves of pitch frequency versus carriage position were made for each spring, and correction factors were established for each model to account for the difference in pitching inertia between each model and the calibration bar.

The effective inertia of the spring-torque tube combinations were determined over the effective lengths of both springs by vibrating the system at a number of carriage positions with and without the calibration bar. The frequency equations were then solved for the effective mass moments of inertia of the spring torque tube combinations at the respective carriage positions.

TABLE III

MODEL MASS AND ELASTIC CHARACTERISTICS

| MODEL | ITEM* | STATION WIDTH (See Station Layout on FIG. A1.2) | | | | | | | | | |
|---|---|---|---|---|---|---|---|---|---|---|---|
| | | 0 - 0.8 | 0.8 - 2.9 | 2.9 - 3.6 | 3.6 - 4.35 | 4.35 - 7.25 | 7.25 - 10.15 | 10.15 - 13.05 | 13.05 - 15.95 | 15.95 - 18.85 | 18.85 - TIP |
| | $b^+$ | 5.22 | 5.03 | 4.85 | 4.80 | 4.52 | 4.14 | 3.76 | 3.38 | 3.00 | 2.64 |
| 1 | EI | 436,000 | 77,000 | 255,100 | 74,000 | 61,500 | 46,000 | 31,300 | 20,700 | 11,100 | 5,000 |
| | GJ | 469,000 | 49,000 | 218,700 | 61,000 | 47,500 | 32,200 | 22,000 | 15,400 | 12,800 | 11,100 |
| | Wt | .1590 | .1300 | .1110 | .1020 | .0400 | .0335 | .0283 | .0222 | .0182 | .016 |
| | $I_\alpha$ | .103 | .169 | .226 | .225 | .200 | .141 | .096 | .062 | .040 | .038 |
| | $x_\alpha$ | --- | --- | --- | --- | .17 | .17 | .17 | .17 | --- | --- |
| 2 | EI | 436,000 | 76,800 | 255,800 | 85,000 | 66,000 | 47,200 | 33,000 | 21,000 | 13,000 | 7,800 |
| | GJ | 469,000 | 48,900 | 217,800 | 57,000 | 47,500 | 36,500 | 26,200 | 18,000 | 13,000 | 9,900 |
| | Wt | .1590 | .1310 | .1100 | .1020 | .0400 | .0335 | .0283 | .0222 | .0182 | .016 |
| | $I_\alpha$ | .103 | .169 | .226 | .225 | .200 | .141 | .096 | .062 | .040 | .038 |
| | $x_\alpha$ | --- | --- | --- | --- | .176 | .176 | .176 | .176 | --- | --- |
| 3 | EI | 436,000 | 52,000 | 358,500 | 65,000 | 50,000 | 35,500 | 24,700 | 16,000 | 10,300 | 6,000 |
| | GJ | 469,000 | 68,000 | 212,800 | 40,500 | 30,000 | 21,000 | 15,400 | 11,200 | 7,700 | 4,700 |
| | Wt | .123 | .119 | .112 | .108 | .042 | .035 | .028 | .023 | .019 | .016 |
| | $I_\alpha$ | .153 | .142 | .143 | .147 | .214 | .151 | .105 | .066 | .043 | .038 |
| | $x_\alpha$ | --- | --- | --- | --- | .18 | .175 | .169 | .17 | --- | --- |
| 4 | EI | 436,000 | 49,000 | 358,500 | 62,200 | 48,500 | 34,000 | 22,500 | 14,600 | 9,500 | 6,000 |
| | GJ | 469,000 | 56,000 | 212,800 | 47,000 | 30,000 | 19,700 | 14,000 | 9,700 | 6,700 | 5,000 |
| | Wt | .123 | .120 | .114 | .110 | .043 | .035 | .029 | .024 | .020 | .017 |
| | $I_\alpha$ | .145 | .140 | .143 | .147 | .210 | .149 | .103 | .067 | .043 | .040 |
| | $x_\alpha$ | --- | --- | --- | --- | .23 | .168 | .167 | .167 | --- | --- |
| 5 | EI | 436,000 | 114,000 | 255,000 | 65,000 | 67,000 | 53,500 | 33,000 | 20,000 | 12,000 | 7,000 |
| | GJ | 469,000 | 77,800 | 218,500 | 59,000 | 48,000 | 34,800 | 23,000 | 15,100 | 10,600 | 7,000 |
| | Wt | .165 | .139 | .118 | .109 | .04 | .0335 | .0283 | .0222 | .0182 | .016 |
| | $I_\alpha$ | .103 | .169 | .226 | .225 | .2 | .141 | .096 | .062 | .040 | .038 |
| | $x_\alpha$ | --- | --- | --- | --- | .19 | .19 | .19 | .19 | --- | --- |
| 6 | EI | 436,000 | 114,000 | 255,000 | 106,000 | 80,000 | 57,200 | 37,800 | 23,800 | 14,000 | 7,000 |
| | GJ | 469,000 | 78,000 | 233,800 | 81,500 | 62,600 | 43,000 | 29,200 | 19,500 | 12,800 | 8,600 |
| | Wt | .165 | .139 | .118 | .109 | .04 | .0335 | .0283 | .0222 | .0182 | .016 |
| | $I_\alpha$ | .103 | .169 | .226 | .225 | .2 | .141 | .096 | .062 | .040 | .038 |
| | $x_\alpha$ | --- | --- | --- | --- | .158 | .158 | .158 | .158 | --- | --- |
| 7 | EI | 436,000 | 49,000 | 358,500 | 64,700 | 50,000 | 34,500 | 23,100 | 14,500 | 9,000 | 5,000 |
| | GJ | 469,000 | 61,000 | 212,800 | 38,500 | 29,500 | 21,200 | 15,300 | 11,000 | 7,700 | 5,500 |
| | Wt | .124 | .119 | .112 | .107 | .036 | .030 | .024 | .019 | .0155 | .014 |
| | $I_\alpha$ | .146 | .141 | .141 | .144 | .181 | .129 | .088 | .056 | .036 | .034 |
| | $x_\alpha$ | --- | --- | --- | --- | .155 | .158 | .167 | .178 | --- | --- |
| 8 | EI | 436,000 | 50,500 | 358,500 | 66,000 | 50,700 | 35,500 | 24,000 | 15,200 | 9,700 | 6,000 |
| | GJ | 469,000 | 57,000 | 212,800 | 39,500 | 31,500 | 23,000 | 16,500 | 11,500 | 8,000 | 5,500 |
| | Wt | .123 | .120 | .114 | .110 | .034 | .029 | .024 | .019 | .016 | .014 |
| | $I_\alpha$ | .144 | .138 | .137 | .139 | .172 | .123 | .084 | .054 | .035 | .033 |
| | $x_\alpha$ | --- | --- | --- | --- | .2 | .157 | .161 | .176 | --- | --- |
| 9 | EI | 436,000 | 66,000 | 358,500 | 69,000 | 54,700 | 38,500 | 26,300 | 17,000 | 10,800 | 6,800 |
| | GJ | 469,000 | 68,000 | 212,800 | 46,000 | 35,000 | 26,000 | 19,000 | 13,500 | 9,200 | 6,500 |
| | Wt | .120 | .116 | .109 | .105 | .033 | .028 | .023 | .019 | .016 | .014 |
| | $I_\alpha$ | .162 | .154 | .151 | .153 | .170 | .122 | .083 | .054 | .034 | .032 |
| | $x_\alpha$ | --- | --- | --- | --- | .25 | .162 | .159 | .168 | --- | --- |
| 10 | EI | 436,000 | 83,000 | 358,500 | 94,000 | 73,500 | 51,500 | 35,500 | 23,000 | 15,000 | 9,000 |
| | GJ | 469,000 | 76,000 | 212,800 | 63,500 | 59,000 | 36,000 | 26,500 | 18,700 | 12,700 | 7,500 |
| | Wt | .124 | .120 | .113 | .109 | .039 | .032 | .027 | .021 | .017 | .016 |
| | $I_\alpha$ | .186 | .170 | .162 | .163 | .187 | .134 | .091 | .059 | .037 | .034 |
| | $x_\alpha$ | --- | --- | --- | --- | .15 | .159 | .156 | .145 | --- | --- |

* b = in.; EI = lb $in.^2$; GJ = lb $in.^2$; Wt = lb/in.; I = lb $in.^2$/in.

\+ Values for b measured perpendicular to E.A. prior to cut out at root and tip.

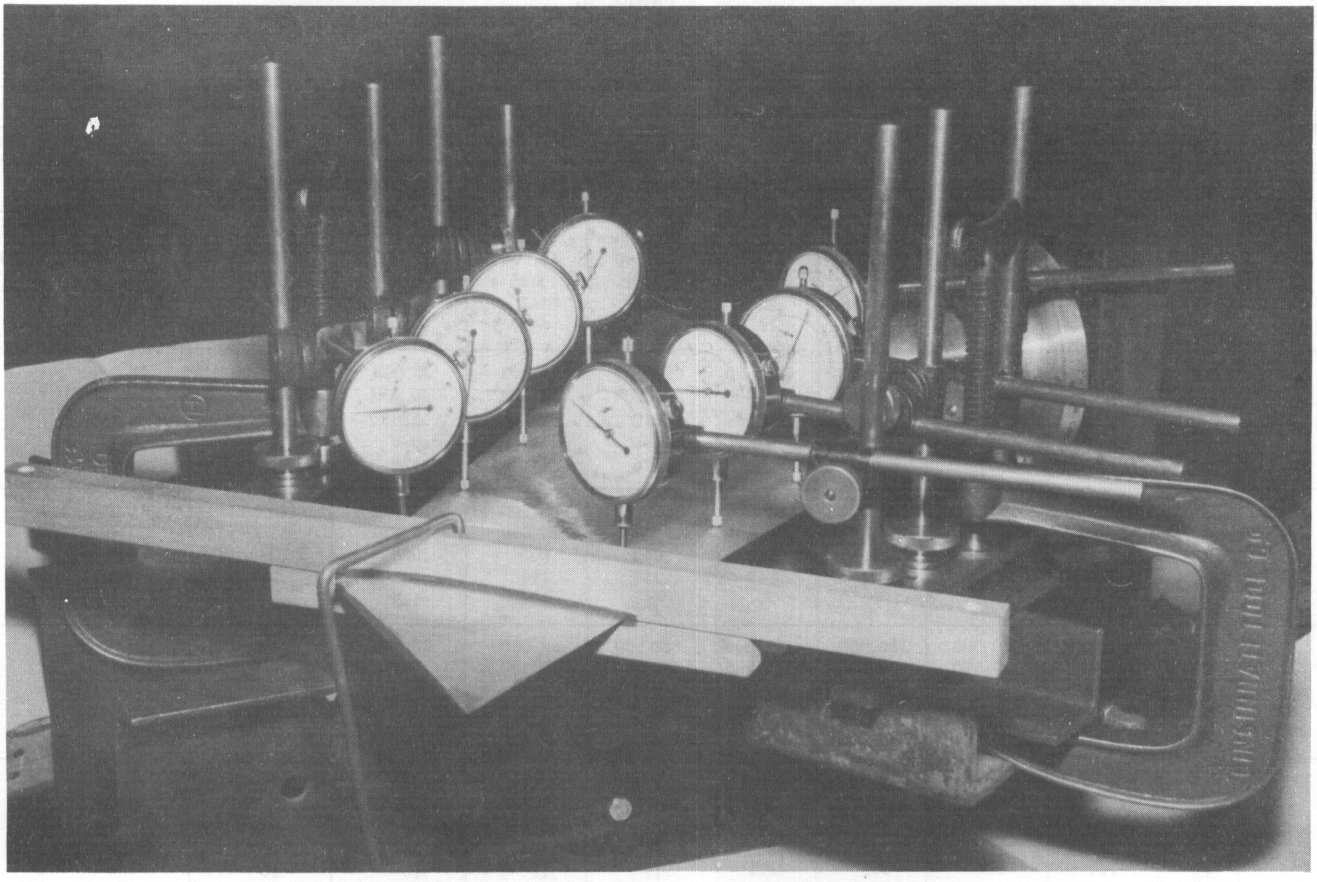

Figure 24. Stabilizer model set-up for static test with loading bar at Station 17.4 and dial indicators at four inboard stations for measurement of bending and twisting displacements.

Figure 25 shows the ratio of the pitching inertia of all elements of the pitch system behind the fuselage fairing to the pitching inertia of the average stabilizer surface outside the fuselage. Figure 25 contains a table which shows the factor by which each model deviates from the plotted data where minimum weight ballasting was employed. For the pitch to bending frequency ratios used during test, the inertia ratios in all cases remained between 0.087 and 0.1171.

To determine the stiffness of the torque tube support system against roll, a rigid aluminum bar with the rolling inertia of the stabilizers was cantilevered from the torque tube. The roll frequency of this system was found to be 258 cps with an effective roll axis 7.5 inches behind the fuselage fairing. Zero air speed analyses performed with and without the roll degree of freedom showed that roll had a negligible effect on the stabilizer model coupled frequencies, but did influence the node line locations of the higher modes of vibration to some extent. Since the roll frequency was roughly 2.5 times the highest flutter frequencies encountered, roll was not included in the flutter analyses.

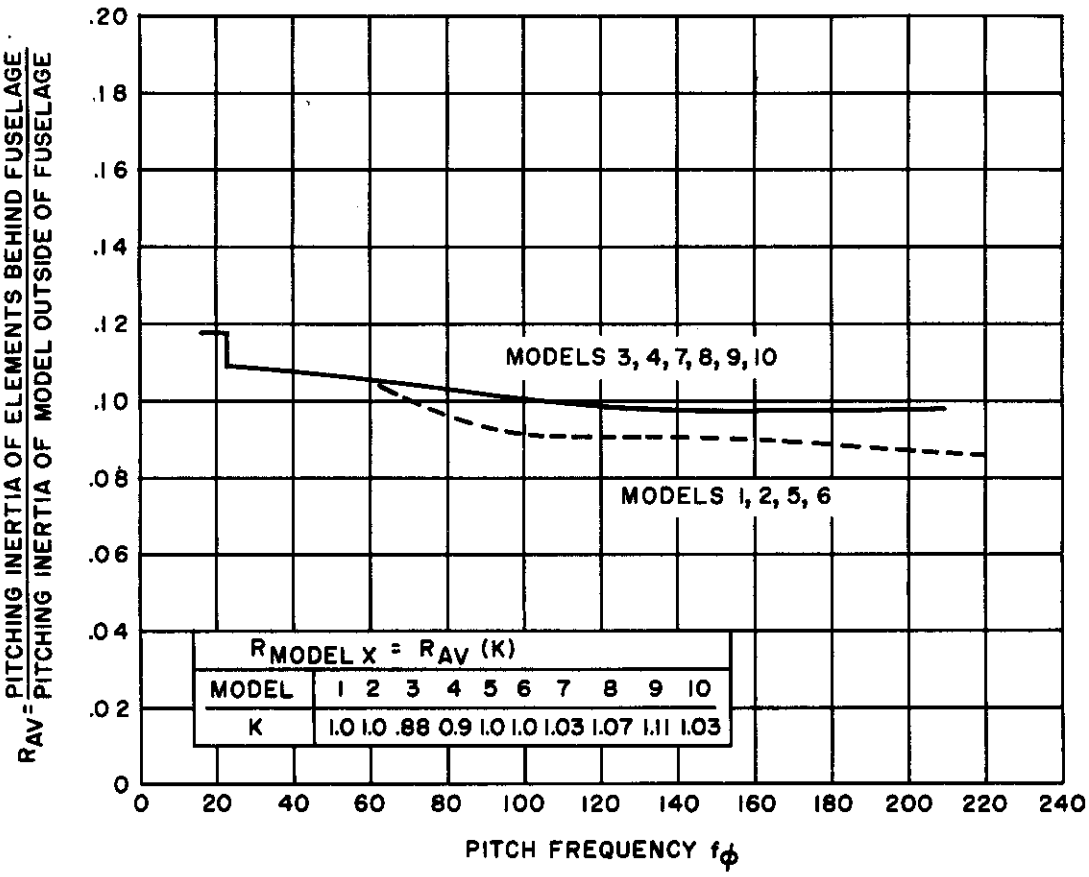


Figure 25. Ratio of the total pitching inertia of all elements of pitch system behind fuselage fairing to the pitching inertia of the stabilizer surface outside of the fuselage fairing.

4. Model Natural Frequency Characteristics

a. Computed Uncoupled Frequencies

The mass and elastic characteristics of the models given in Table III were established by the methods indicated in Appendix II-1 and II-2. This data was used for the computation of the uncoupled bending frequencies using Thompson's method and uncoupled torsion frequencies using the Holzer method. The uncoupled frequencies thus obtained are listed in Table I, "Summary of Model Characteristics". Bending to torsion frequency ratios deviated only slightly from 0.273.

b. Computed Coupled Frequencies and Node Lines

The mass and elastic data established in the foregoing Sections of Appendix II were employed in zero airspeed analyses over the range of pitch frequencies of interest to establish coupled frequency ratios and node lines. The first and second bending, torsion, pitch, and roll modes were included in the analysis. Node lines for the first three modes were computed at intervals over the range of pitch to bending frequency ratios of interest. Analysis node lines at pitch to bending frequency ratios of 0.9, 1.5 and 2.67 are shown in Figure 26 as dotted lines. Figures 27-29 show the analytically predicted variations in the coupled to torsion frequency ratio with pitch to torsion frequency ratio for the first three coupled modes.

c. Experimental Coupled Frequencies and Node Lines

In the laboratory, node lines and coupled frequencies for the first three modes of vibration were obtained over the range of available pitch frequencies. The observed node lines for Models 2, 4, 6, 8 and 10 have been plotted on Figure 26 for pitch to bending frequency ratios of 0.9, 1.5 and 2.67 as solid lines for comparison with the analytically predicted values shown as dash lines.

The observed coupled frequencies were ratioed with the uncoupled torsion frequencies of the respective models and were then plotted versus pitch to torsion frequency ratio in Figures 27 - 29 for comparison with analytically predicted values. The general agreement between analysis and measured characteristics is taken as substantiation of the mass and elastic characteristics given in Tables I and III.

d. Instrumentation Calibrations

Oscillograph records of strain gage response were used to determine model natural coupled frequencies, flutter frequencies and flutter mode shapes. Bending moment and torque sensitive bridges were located along the elastic axis of the model and a strain gage bridge was placed on the pitch flexure pivot springs. The latter bridge was calibrated directly in terms of pitch displacement of the stabilizer torque tube. The bridges on the models were calibrated in terms of bridge response to bending moments and torques at the respective bridges. Calibrations were also run to determine bridge temperature sensitivity. These calibrations allowed the determination of bending moments and torques at the bridge locations on the models during flutter. This information was converted to tip amplitude ratios using the basic methods of Section A 3.13 of WADC TR 53-47 (Reference 2) which assumes that the flutter mode can be represented by the superposition (with proper phasing) of normal modes of vibration.

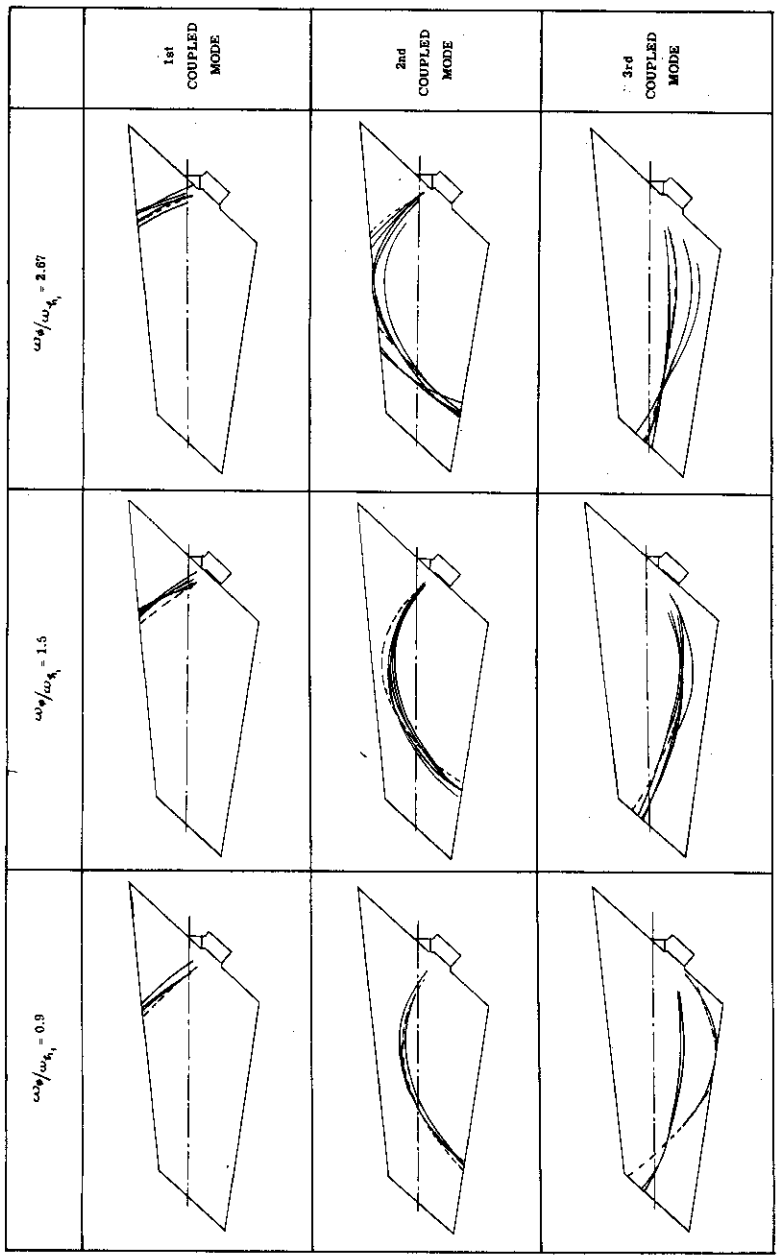


Figure 26. Node lines for the first three coupled modes observed in the laboratory on models 2, 4, 6, 8 and 10 at pitch to torsion frequency ratios of 0.9, 1.5 and 2.67. Values predicted by analysis are shown as dotted lines.

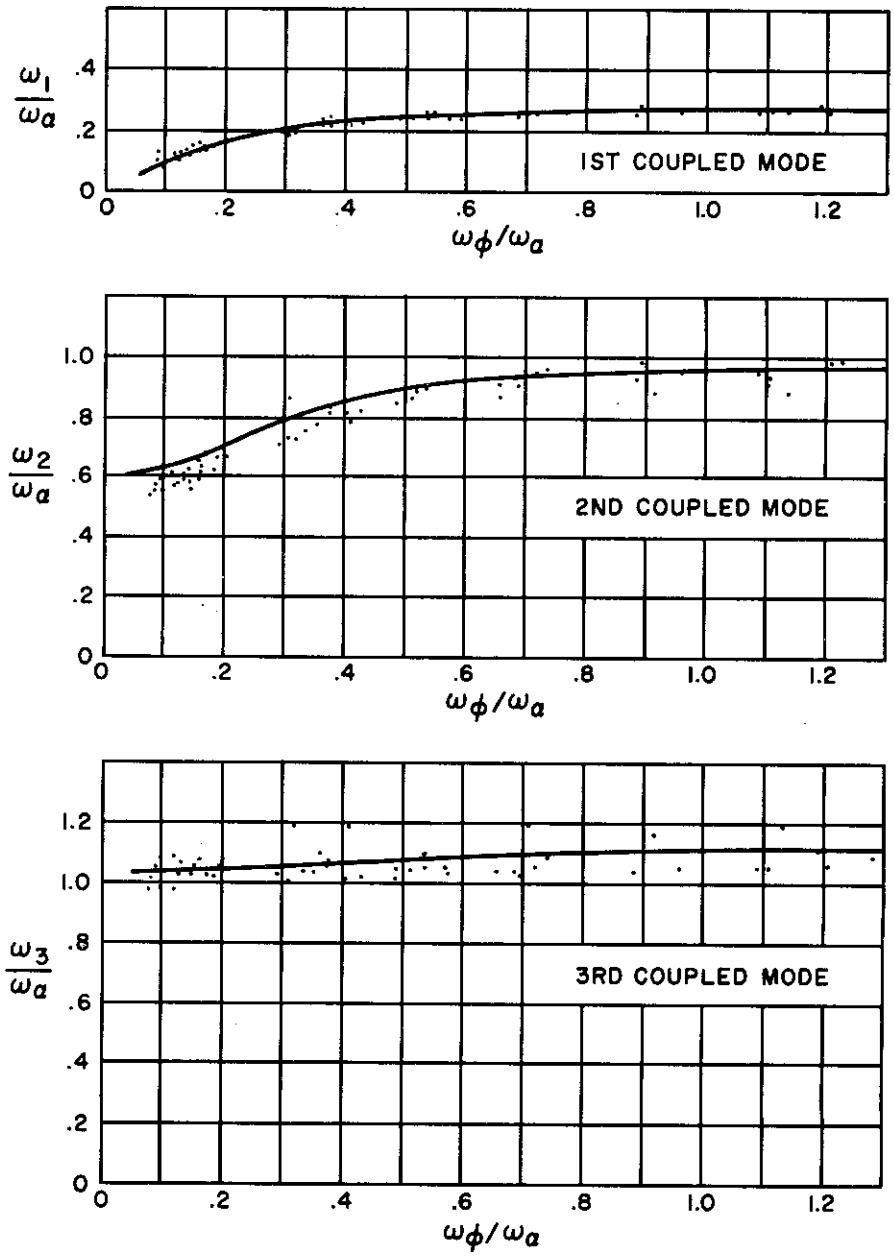


Figure 27. Ratio of coupled to first torsion frequency vs pitch to torsion frequency ratio. Solid line represents analysis results. Dots indicate data obtained in the laboratory for each of the 10 models.

APPENDIX III

FLUTTER ANALYSES DETAILS

1. Flutter Equations

Flutter analyses for the models of this program employed the methods of Reference 1 expanded to four degrees of freedom by the addition of pitch and second bending. Using the notation of Figure 28 the displacements h (positive down) of any point on the elastic axis and rotation $\alpha$ about the elastic axis (positive with leading edge up) due to pitch plus the elastic degrees of freedom will be

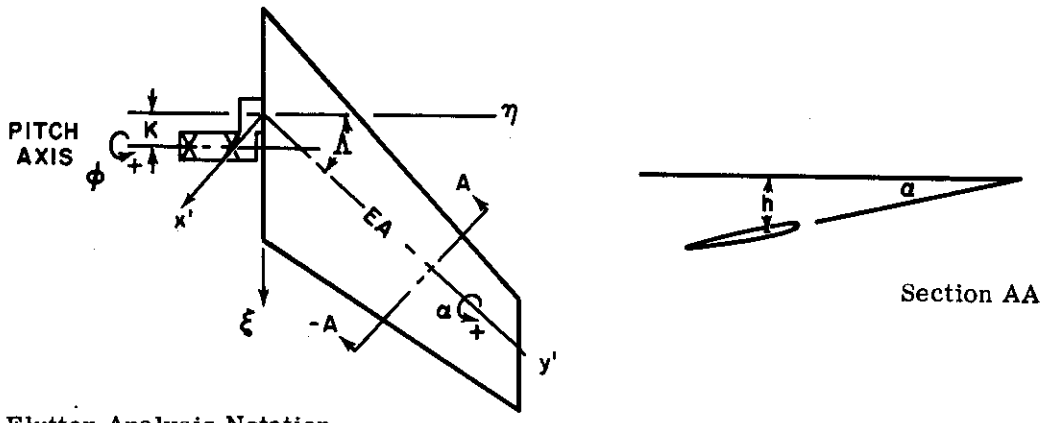


Figure 28. Flutter Analysis Notation

given by $h = \phi y \sin \Lambda - K\phi + f_{h_1} \underline{h}_1 + f_{h_2} \underline{h}_2$

and $\alpha = \phi \cos \Lambda + f_\alpha \underline{\alpha}$

Substituting these values of h and $\alpha$ for the corresponding values given in equations (12) of Reference 1 and proceeding as usual, the flutter determinant elements may be written as indicated in Table IV where the flutter equations are:

$$A_{h_1 h_1} \underline{h_1} + A_{h_1 \alpha} \underline{\alpha} + A_{h_1 \phi} \underline{\phi} + A_{h_1 h_2} \underline{h_2} = 0$$

$$A_{\alpha h_1} \underline{h_1} + A_{\alpha \alpha} \underline{\alpha} + A_{\alpha \phi} \underline{\phi} + A_{\alpha h_2} \underline{h_2} = 0$$

$$A_{\phi h_1} \underline{h_1} + A_{\phi \alpha} \underline{\alpha} + A_{\phi \phi} \underline{\phi} + A_{\phi h_2} \underline{h_2} = 0$$

$$A_{h_2 h_1} \underline{h_1} + A_{h_2 \alpha} \underline{\alpha} + A_{h_2 \phi} \underline{\phi} + A_{h_2 h_2} \underline{h_2} = 0$$

The aerodynamic coefficients $A_{ch}$, $A_{c\alpha}$, $A_{\alpha h}$, $A_{\alpha\alpha}$, $A_{c\tau}$ and $A_{\alpha\tau}$ included in the determinant elements are defined in Reference 1. Other symbols are defined in the list of symbols at the front of the report.

## 2. Mass and Elastic Characteristics Used in Analyses

Flutter analyses were run in dimensional form using the actual mass characteristics of Model 1, Table III, and the mode shapes shown in Figure 29. The desired ranges in $\mu$ and $x_\alpha$ were, of course, obtained by appropriate variations in $\rho$ and $S_\alpha$. Since the models were constructed and ballasted to have common non-dimensional flutter parameters, the characteristics of Model 1 were representative of the whole series. Figure 25 shows that pitching inertias of those elements behind the fuselage fairing varied only slightly from 10 percent of the stabilizer pitching inertia. For the analyses, then, the total pitching inertia was taken as 110 percent of the average stabilizer pitching inertia of 20.53 given in Table I.

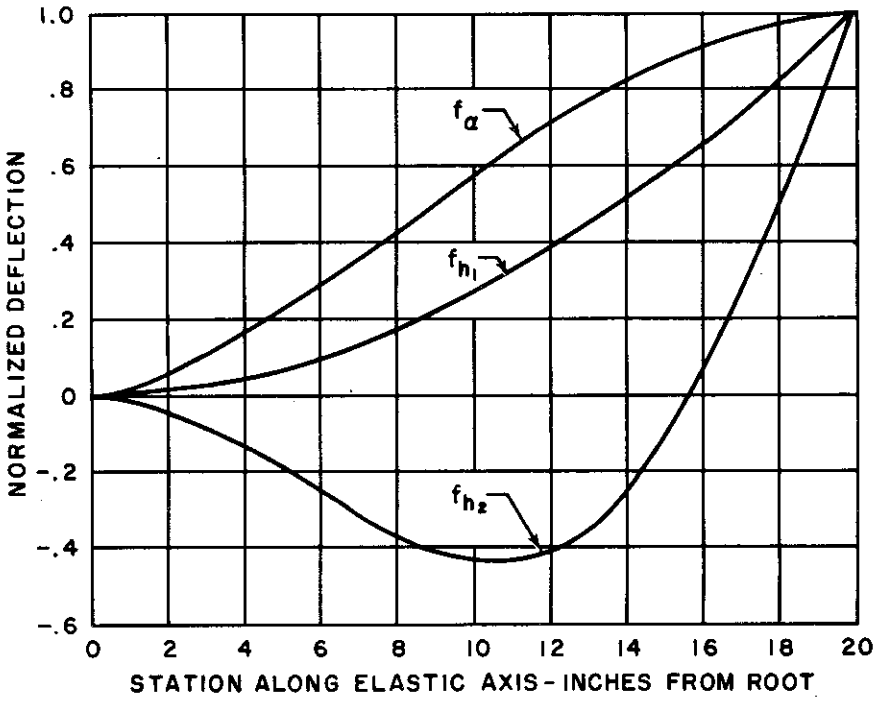


Figure 29. Mode shapes in bending and torsion used in flutter analysis.

TABLE IV

DETERMINANT ELEMENTS USED IN FLUTTER ANALYSIS

$$A_{h_1h_1} = \left[1-(\omega_{h_1}/\omega_\alpha)^2\Omega\right]\int_0^1 m\, f_{h_1}^2\, dy - \pi\rho\left[\int_0^1 b^2 A_{ch}\, f_{h_1}^2\, dy - \tan\Lambda\int_0^1 b^3 (i/k_n) A_{ch}\, f_{h_1}\, df_{h_1}/dy\, dy\right]$$

$$A_{h_1\alpha} = \int_0^1 S_\alpha f_{h_1} f_\alpha\, dy - \pi\rho\left[\int_0^1 b^3 A_{c\alpha} f_{h_1} f_\alpha\, dy + \tan\Lambda\int_0^1 b^4 A_{cT} f_{h_1}\, df_\alpha/dy\, dy\right]$$

$$A_{h_1\phi} = \sin\Lambda\int_0^1 m f_{h_1} f_\phi y\, dy + \cos\Lambda\int_0^1 S_\alpha f_{h_1} f_\phi\, dy - K\int_0^1 m f_{h_1} f_\phi\, dy - \pi\rho\left[\sin\Lambda\int_0^1 b^2 A_{chy} f_{h_1} f_\phi dy - \sin\Lambda\tan\Lambda\int_0^1 b^3 (i/k_n) A_{ch} f_{h_1} f_\phi\, dy + \cos\Lambda\int_0^1 b^3 A_{c\alpha} f_{h_1} f_\phi\, dy - K\int_0^1 b^2 A_{ch} f_{h_1} f_\phi\, dy\right]$$

$$A_{h_1h_2} = \int_0^1 m f_{h_1} f_{h_2} dy - \pi\rho\left[\int_0^1 b^2 A_{ch} f_{h_1} f_{h_2}\, dy - \tan\Lambda\int_0^1 b^3 (i/k_n) A_{ch} f_{h_1}\, df_{h_2}/dy\, dy\right]$$

$$A_{\alpha h_1} = \int_0^1 S_\alpha f_\alpha f_{h_1} dy - \pi\rho\left[\int_0^1 b^3 A_{ah} f_\alpha f_{h_1}\, dy - \tan\Lambda\int_0^1 b^4 (i/k_n) A_{ah} f_\alpha\, df_{h_1}/dy\, dy\right]$$

$$A_{\alpha\alpha} = (1-\Omega)\int_0^1 I_\alpha f_\alpha^2\, dy - \pi\rho\left[\int_0^1 b^4 A_{a\alpha} f_\alpha^2 dy + \tan\Lambda\int_0^1 b^5 A_{aT} f_\alpha\, df_\alpha/dy\, dy\right]$$

$$A_{\alpha\phi} = \sin\Lambda\int_0^1 S_\alpha f_\alpha f_\phi\, y\, dy + \cos\Lambda\int_0^1 I_\alpha f_\alpha f_\phi\, dy - K\int_0^1 S_\alpha f_\alpha f_\phi\, dy - \pi\rho\left\{\sin\Lambda\int_0^1 \left[b^3 A_{ahy} - b^4 (i/k_n)\tan\Lambda A_{ah}\right] f_\alpha f_\phi\, dy + \cos\Lambda\int_0^1 A_{a\alpha} b^4 f_\alpha f_\phi\, dy - K\int_0^1 b^3 A_{ah} f_\alpha f_\phi\, dy\right\}$$

$$A_{\alpha h_2} = \int_0^1 S_\alpha f_\alpha f_{h_2}\, dy - \pi\rho\left[\int_0^1 b^3 A_{ah} f_\alpha f_{h_2}\, dy - \int_0^1 b^4 (i/k_n)\tan\Lambda A_{ah} f_\alpha\, df_{h_2}/dy\, dy\right]$$

$$A_{\phi h_1} = \sin\Lambda\int_0^1 m f_\phi f_{h_1}\, y\, dy + \cos\Lambda\int_0^1 S_\alpha f_\phi f_{h_1}\, dy - K\int_0^1 m f_\phi f_{h_1}\, dy - \pi\rho\left\{\sin\Lambda\int_0^1 \left[b^3 A_{ch} f_{h_1} - b^3 (i/k_n)\tan\Lambda A_{ch}\, df_{h_1}/dy\right] y\, f_\phi\, dy + \cos\Lambda\int_0^1 \left[b^3 A_{ah} f_{h_1} - b^4 (i/k_n)\tan\Lambda A_{ah}\, df_{h_1}/dy\right] f_\phi\, dy - K\int_0^1 \left[b^2 A_{ch} f_{h_1} - b^3 (i/k_n)\tan\Lambda A_{ch}\, df_{h_1}/dy\right] f_\phi\, dy\right\}$$

$$A_{\phi\alpha} = \sin\Lambda\int_0^1 S_\alpha f_\phi f_\alpha y\, dy + \cos\Lambda\int_0^1 I_\alpha f_\phi f_\alpha\, dy - K\int_0^1 S_\alpha f_\phi f_\alpha\, dy - \pi\rho\left\{\sin\Lambda\int_0^1 \left[b^3 A_{c\alpha} f_\alpha + b^4\tan\Lambda A_{cT}\, df_\alpha/dy\right] y\, f_\phi\, dy + \cos\Lambda\int_0^1 \left[b^4 A_{a\alpha} f_\alpha + b^5\tan\Lambda A_{aT}\, df_\alpha/dy\right] f_\phi\, dy - K\int_0^1 \left[b^3 A_{c\alpha} f_\alpha + b^4\tan\Lambda A_{cT} df_\alpha/dy\right] f_\alpha dy\right\}$$

$$A_{\phi\phi} = \left[1-(\omega\phi/\omega_\alpha)^2\Omega\right]\left[\sin^2\Lambda\int_0^1 m f_\phi^2 y^2\, dy + 2\sin\Lambda\cos\Lambda\int_0^1 S_\alpha f_\phi^2\, y\, dy + \cos^2\Lambda\int_0^1 I_\alpha f_\phi^2\, dy - 2K\sin\Lambda\int_0^1 m f_\phi^2\, y\, dy + K^2\int_0^1 m f_\phi^2\, dy - 2K\cos\Lambda\int_0^1 S_\alpha f_\phi^2\, dy\right] - \pi\rho\left\{\sin^2\Lambda\int_0^1 \left[b^2 A_{ch} y^2 - b^3 (i/k_n)\tan\Lambda A_{ch} y\right] f_\phi^2 dy + \sin\Lambda\cos\Lambda\int_0^1 \left[b^3 y (A_{ah}+A_{c\alpha}) - b^4 (i/k_n)\tan\Lambda A_{ah}\right] f_\phi^2 dy + \cos^2\Lambda\int_0^1 b^4 A_{a\alpha} f_\phi^2\, dy - K\sin\Lambda\int_0^1 \left[2y b^2 A_{ch} - b^3 (i/k_n)\tan\Lambda A_{ch}\right] f_\phi^2 dy - K\cos\Lambda\int_0^1 b^3 (A_{ah}+A_{c\alpha}) f_\phi^2 dy + K^2\int_0^1 b^3 A_{ch} f_\phi^2\, dy\right\}$$

[redacted]

$$A_{\phi h_2} = \sin\Lambda \int_o^L m f_\phi f_{h_2} y\, dy + \cos\Lambda \int_o^L S_\alpha f_\phi f_{h_2} dy - K\int_o^L m f_\phi f_{h_2} dy - \pi\rho\{\sin\Lambda\int_o^L [b^2 A_{ch} f_{h_2} - b^3(i/k_n)\tan\Lambda A_{ch} df_{h_2}/dy] y f_\phi dy + \cos\Lambda\int_o^L [b^3 A_{ah} f_{h_2} - b^4(i/k)\tan\Lambda A_{ah} df_{h_2}/dy] f_\phi dy - K\int_o^L [b^2 A_{ch} f_{h_2} - b^3(i/k_n)\tan\Lambda A_{ch}\, df_{h_2}/dy]\, f_\phi\, dy\}$$

$$A_{h_2 h_1} = \int_o^L m f_{h_2} f_{h_1} dy - \pi\rho[\int_o^L b^2 A_{ch} f_{h_2} f_{h_1} dy - \tan\Lambda \int_o^L b^3(i/k_n)\, A_{ch}\, f_{h_2}\, df_{h_1}/dy\, dy$$

$$A_{h_2\alpha} = \int_o^L S_\alpha f_{h_2} f_\alpha dy - \pi\rho\,[\int_o^L b^3\, A_{c\alpha} f_{h_2} f_\alpha\, dy + \int_o^L b^4 \tan\Lambda\, A_{cT} f_{h_2} df_\alpha/dy\, dy$$

$$A_{h_2\phi} = \sin\Lambda\int_o^L m f_{h_2} f_\phi\, y\, dy + \cos\Lambda\int_o^L S_\alpha f_{h_2} f_\phi\, dy - K\int_o^L m f_{h_2} f_\phi\, dy - \pi\rho[\sin\Lambda\int_o^L b^2 A_{ch} y\, f_{h_2} f_\phi\, dy - \sin\Lambda\tan\Lambda\int_o^L b^3(i/k_n) A_{ch} f_{h_2} f_\phi\, dy + \cos\Lambda\int_o^L b^3 A_{c\alpha} f_{h_2} f_\phi\, dy - K\int_o^L b^2 A_{ch}\, f_{h_2} f_\phi\, dy\,]$$

$$A_{h_2 h_2} = [1 - (\omega_{h_2}/\omega_\alpha)^2 \Omega]\int_o^L m f_{h_2}^2\, dy - \pi\rho[\int_o^L b^2 A_{ch}\, f_{h_2}^2\, dy - \tan\Lambda\int_o^L b^3(i/k_n) A_{ch} f_{h_2} df_{h_2}/dy\, dy$$



[redacted]